

Behavior of Na and Cs vapors confined in nanometric-thin cells

Theory and experiments

Rodolphe MOMIER

Master PPN - Physics, Photonics and Nanotechnology

June 4, 2021

Supervised by:

Prof. Aram PAPOYAN

Institute for Physical Research
National Academy of Sciences of Armenia
Ashtarak-2, 0203, Armenia

Prof. Claude LEROY

Laboratoire Interdisciplinaire Carnot de Bourgogne
UMR CNRS 6303 - Université Bourgogne Franche-Comté
9 avenue Alain Savary, F-21078 Dijon, France



Laboratoire Interdisciplinaire
Carnot de Bourgogne



Acknowledgements

First of all, I would like to address my utmost gratitude to my supervisor here in Armenia, Prof. Aram PAPOYAN, for being such an awesome teacher and for spending so much time with me despite his extremely busy schedule. The discussions we had were always extremely interesting, and I am convinced I am leaving Armenia as a better young physicist than I was a few months ago.

I address my deepest thanks to Prof. Claude LEROY for believing in my abilities since we started working together during my bachelor in 2019. It has been a real pleasure to work ever since, and it eventually led to me being here in Armenia as I write these few words. I certainly would not be where (and who) I am today without his precious help.

My warmest thanks go to Mrs. Pauline MARCEAU, who surely did her best to organize this trip to Armenia. I also would like to thank Graduate School EIPHI-UBFC for its financial support through the "Alliance" program as well as Région Bourgogne Franche-Comté through the program "Dynastage".

I am deeply thankful to Dr. Armen SARGSYAN for everything he did to assist me during my stay in Armenia. From picking me up at the airport to allowing me to participate in experimental sessions, all the support, be it professional or personal, was of great help throughout these few months. To him and his family, I wish all the best.

Of course, one cannot spend time at the Institute for Physical Research without meeting Prof. David SARKISYAN. I sincerely thank him for all the time we spent in his office, discussing different aspects of atomic physics, and for giving me the opportunity to confront the theory I have been studying with the reality of experiments (and luckily, it works!).

I warmly thank all the people I had the opportunity to meet here for the warm welcome I received. To name a few: Dr. Arevik AMIRYAN-KLINGER, Dr. Ara TONOYAN, Dr. Emil GAZAZYAN, Dr. Svetlana SHMAVONYAN and Dr. Vanik "vem" MKRTCHYAN. I sincerely thank Dr. Emmanuel KLINGER for the stimulating discussions we had concerning the theoretical part of this manuscript, even though we did not have the opportunity to meet face to face. I also thank Artur ALEKSANYAN whom I have been working with for the past two years.

Contents

1	Introduction	1
1.1	Generalities	1
1.2	Alkali electronic structure	2
1.3	Properties of alkali vapors	2
1.4	Nanometric-thin cells	3
2	Spectroscopy of nanometric-thin alkali vapors	5
2.1	Theoretical model	5
2.2	Sub-Doppler spectroscopy of a 400 nm-thick cesium vapor at room temperature	7
3	Influence of an external magnetic field	8
3.1	Theoretical model	8
3.2	Sub-Doppler spectra of sodium <i>D</i> lines in a wide range of magnetic field	10
Conclusion and outlook		23
A	Additional information	24
B	Linear interaction regime	26

List of Figures

1.1	Vapor pressure versus temperature	3
1.2	Doppler broadening versus temperature	3
1.3	Scheme of a nanocell	4
1.4	Picture of a nanocell	4
2.1	Illumination of the nanocell	5
2.2	Scheme of a two-level system	5
2.3	Two-level medium transmission lineshape in the linear interaction regime	7
2.4	Two-level medium SR lineshape in the linear interaction regime	7
3.1	Sodium ground Zeeman structure	10
3.2	Sodium D_2 excited Zeeman structure	10
A.1	Sodium and cesium D lines fine and hyperfine structures	24
A.2	Sapphire refractive index curve	24

Chapter 1

Introduction

1.1 Generalities

Alkali metal atoms are widely used objects in atomic physics for a wide number of reasons. In terms of experiment, their convenience is due to the high density of atomic vapor at relatively low temperatures, and the presence of strong optical transitions from the ground state (D_1 and D_2 lines) in the visible or near infrared region of the spectrum, for which relatively cheap cw lasers are available. From a theoretical point of view, they are attractive due to simplicity of their energy levels caused by the presence of a single valence electron which significantly facilitates the calculations, so that spectroscopic data are now very well documented [1–7]. Magneto-optical phenomena in alkali metal vapors are of particular interest. Complete understanding of various magneto-optical effects occurring in alkali vapors [8] is important since they are widely used, for example in fundamental and applied studies of electromagnetically induced transparency [9, 10], Faraday filters [11, 12], optical magnetometry [13], laser-frequency locking [14] and elsewhere. Such phenomena often rely on the peculiarities of the behavior of Zeeman transitions, so that frequency separation of individual transitions is of high importance. Meanwhile for a vapor media, the thermal motion of atoms resulting in Doppler broadening leads to overlapping of hyperfine transitions and their Zeeman components, thus limiting its spectroscopic applicability. Significant sub-Doppler narrowing of atomic transitions can be attained with the use of so-called optical nanocells [15–17]. Being enclosed in optical cells with a thickness commensurable with the resonant wavelength, alkali metal vapors become a powerful tool for the high-resolution atomic spectroscopy, opening new possibilities for studying magneto-optical processes, where spectral resolution of individual transitions between magnetic sublevels (Zeeman transitions) is essential. Complete determination of the behavior of all the possible individual Zeeman transitions can be done using a well-known theoretical model first provided by Tremblay *et al.* [18]. Importantly, besides frequency splitting in magnetic field, Zeeman transitions undergo also significant probability changes [17]. This allows to observe the appearance of several peculiarities, such as Guiding Transitions (GT) and two different types of so-called Magnetically-induced Circular Dichroism (MCD) [19, 20]. Moreover, several efficient techniques have been developed to enhance a spectral visibility of Zeeman transitions while preserving their relative probability scaling, such as derivative of Selective Reflection (dSR) [13, 21] and Second Derivative of absorption (SD) [22–24].

Most of the experimental studies were done using rubidium and cesium atomic vapor due to the availability of relatively inexpensive cw diode lasers operating in their resonant wavelength range. For these atoms, also the hyperfine splitting is affordably large (the lowest frequency separation between adjacent upper states is ≈ 30 MHz for ^{85}Rb). The magneto-optical effects on sodium D_1 and D_2 lines have been much less studied. The reason for this is the lack of convenient inexpensive lasers operating in the region of these resonances (589.6 nm and 589.0 nm, respectively), as well as the relatively low vapor density. Although some information concerning Zeeman transitions of sodium exists in the literature [25–27], the available information is far from being complete. Meanwhile, recently interest in magneto-optical processes in sodium vapor has increased. In this report, we provide a complete theoretical description of the behavior of alkali vapors in nanocells, with and without applying an external magnetic field. This manuscript is organized in three main parts:

- This Chapter is a global introduction to nanocells and properties of alkali metal vapors.
- In Chapter 2, we present a theoretical analysis of the transmitted and reflected lineshape through a nanocell. In this model, the nanocell is seen as Fabry-Pérot cavity and the atomic vapor is seen as an ensemble of two-level systems. This model allowed us to compute absorption spectra of cesium and compare with experimental spectra obtained at room temperature.
- In Chapter 3, we study the influence of the external magnetic field on the electronic structure of the atom. This allows to obtain the behavior of every possible Zeeman transition. Combined with the theoretical model developed in Chapter 2, we present for the first time a comprehensive set of theoretical sub-Doppler spectra of sodium D lines for a magnetic field varying up to 1 Tesla, as well as a thorough description of most of the peculiarities that occur. Due to the lack of a laser working in the wavelength range of sodium, we restrict ourselves to theoretical calculations. However, since the quantum system is similar to the one of ^{87}Rb and ^{39}K D lines, we expect a total agreement between our results and upcoming experiments performed with sodium nanocells.

Two articles embodying the results presented in this manuscript have been submitted to two peer-reviewed journals, one being accepted (June 1st, 2021), and the other one being under review.

1.2 Alkali electronic structure

The fine structure of the alkali atom arises from the so-called "spin-orbit coupling", ie. the interaction between the spin momentum and the orbital angular momentum of the electron. This phenomenon is naturally described by the Dirac equation, as it will be presented in Chapter 3. The resulting total electronic angular momentum \mathbf{J} is therefore

$$\mathbf{J} = \mathbf{L} + \mathbf{S}, \quad (1.1)$$

and its magnitude J takes the values $|L - S| \leq J \leq L + S$. Analogously, one can consider the interaction between the total electronic angular momentum and the intrinsic nuclear spin momentum. This coupling gives rise to a total atomic angular momentum \mathbf{F} such that

$$\mathbf{F} = \mathbf{J} + \mathbf{I}, \quad (1.2)$$

with its magnitude F taking the values $|J - I| \leq F \leq J + I$. The fine states (also called S -states) are denoted $n^{2S+1}X_j$, where n (resp. X) denotes the shell (resp. subshell) of the valence electron. The term $2S + 1$ is called the spin degeneracy. Except for the S subshell, the spin-orbit coupling splits the electronic states into $2S + 1$ fine states indexed by the value of J . Similarly, the $\mathbf{J} - \mathbf{I}$ coupling raises the degeneracy of the fine states by splitting them into $2J + 1$ hyperfine states indexed by F . These hyperfine states experience an energy shift [6]

$$\Delta E_{hf} = \frac{A_{hf}}{2} + B_{hf} \frac{\frac{3}{2}K(K+1) - 2I(I+1)J(J+1)}{4I(2I-1)J(2J+1)}, \quad (1.3)$$

where $K = F(F+1) - I(I-1) - J(J-1)$, and A_{hf} (resp. B_{hf}) is the magnetic dipole (resp. electric quadrupole) constant (table A.1).

The so-called D_1 line of an alkali atom corresponds to the optical transition between the fine states $n^2S_{1/2}$ and $n^2P_{1/2}$. In the case of sodium (^{23}Na), the involved states are $3^2S_{1/2}$ and $3^2P_{1/2}$, whereas for cesium (^{133}Cs) the transition occurs between the states $6^2S_{1/2}$ and $6^2P_{1/2}$. For the case of the D_2 line, the excited state is always such that $J = 3/2$, that is $3^2S_{1/2} \rightarrow 3^2P_{3/2}$ for sodium and $6^2S_{1/2} \rightarrow 6^2P_{3/2}$ for cesium. Moreover, sodium has a smaller ($I = 3/2$) nuclear spin momentum than cesium ($I = 7/2$), leading to a different hyperfine structure. The complete fine and hyperfine manifolds of both isotopes' D lines are provided in Appendix A, at the end of this manuscript (figure A.1), along with some key numerical values that will be needed later (table A.1).

1.3 Properties of alkali vapors

Generally, in the low-pressure limit, the vapor pressure P of an atomic gas as a function of the temperature T can be closely approximated by

$$\log_{10}(P) = A + BT^{-1} + C \log_{10} T + DT \cdot 10^{-3}, \quad (1.4)$$

where the parameters A, B, C, D can be found in [28, 29]. The resulting pressure, in mmHg, is presented in figure 1.1 for all alkali except lithium. The number density $N_D = N/V$ can be recovered by the ideal gas law:

$$N_D = \frac{P}{k_B T}. \quad (1.5)$$

In this report, we consider that the alkali vapor is composed of atoms moving with different velocities obeying the Maxwell-Boltzmann distribution

$$W(v) = (v_p \sqrt{\pi})^{-1} \exp\left(-\frac{v^2}{v_p^2}\right). \quad (1.6)$$

With this definition, the atoms' most probable thermal velocity (the peak of the distribution) is given by $v_p = \sqrt{2k_B T / m_a}$ and the mean thermal velocity is $\langle v \rangle = \sqrt{8k_B T / \pi m_a} = 2v_p / \sqrt{\pi}$, where m_a is the atomic mass (in kg). Typically, $\langle v \rangle \approx 218 \text{ m.s}^{-1}$ for cesium atoms at 25 °C and $\langle v \rangle \approx 524 \text{ m.s}^{-1}$ for sodium atoms at 25 °C. Due to the different classes of atomic velocities, the incident laser radiation ω_L is seen by the atoms (ω) as slightly shifted (either towards the blue or the red region of the spectrum) such that

$$\omega = \omega_L - \Delta_D, \quad (1.7)$$

with $\Delta_D = \mathbf{k} \cdot \mathbf{v} = \mp k v_z$, where $k \equiv k_z$ is the laser wavevector propagating perpendicularly to the cell (z -direction), and v_z is the projection of the atomic velocity obeying the distribution defined by equation (1.6). This effect is called the atomic Doppler effect and gives rise to an inhomogeneous broadening of the resonance lines [30]

$$\gamma_D = \omega_0 \sqrt{\frac{8k_B T \ln 2}{m_a c^2}}, \quad (1.8)$$

where c is the speed of light and ω_0 is the angular central frequency of the transition. The Doppler broadening is presented in figure 1.2 for the central angular frequencies of the D_1 and D_2 lines of every alkali except lithium. These frequencies for sodium and cesium are presented in table A.1 at the end of the manuscript.

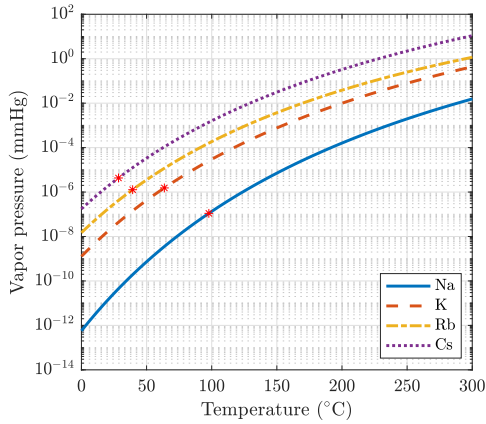


Figure 1.1: Vapor pressure (mmHg) of Na, K, Rb and Cs as a function of the temperature. The red stars show the melting point of each metal.

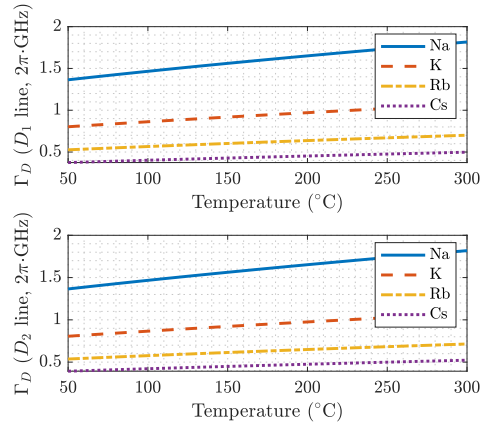


Figure 1.2: Top panel: Doppler broadening computed for the central angular frequency of the D_1 transition of Na, K, Rb and Cs. Bottom panel: computation performed for the D_2 transition.

1.4 Nanometric-thin cells

The nanocells are made of two rectangular garnet ($\text{Y}_3\text{Al}_5\text{O}_{12}$) or sapphire (Al_2O_3) wedged windows. The choice of component is important for the durability of the cell due to the strong chemical aggressiveness of alkali atoms. This aggressiveness increases with temperature so that using a regular glass nanocell heated to more than 200 °C for a few hours would result in complete blackening of the windows due to corrosion. The typical dimensions of the windows are $3 \times 2 \text{ cm}^2$ and a thickness of $\sim 3 \text{ mm}$. To avoid any undesirable effects such as birefringence, the sapphire has to be cut so that its c -axis is perpendicular to the window. The sapphire surface is polished to a roughness smaller than $\lambda/10$ (typically $\lambda/10 \approx 50\text{-}100 \text{ nm}$). A vacuum gap is created between the two windows. This gap is obtained by placing strips of platinum or titanium of different thickness on the top and bottom of the windows, as seen in figure 1.3, so that the thickness L of the cell ranges between a few tens of nanometers to 1 micron. The windows are attached to a side-arm containing Rb, Cs, Na or K (usually solid at room temperature, but an ambient 30 °C is enough to have liquid cesium, as seen in figure 1.1). Everything is glued with high-temperature glue since the nanocells can be heated up to several hundreds of degrees Celsius in order to obtain sufficient number density. Let us note two things: firstly, no nanocell was built containing lithium atoms. Due to their small size, lithium atoms are able to pass through the glue and escape the cell. Secondly, when performing experiments, the cell is usually placed in an oven. The dimensions of the oven strongly depend on the experiment (application of a magnetic field, ...). The side-arm is heated and the temperature is checked by a thermocouple attached to the side-arm. The most important part is to avoid atomic condensation on the windows. To do so, the temperature of the windows is always kept a few tens of degrees higher than the temperature of the sidearm. The refractive index of sapphire is typically in the range 1.7 – 1.8 for the wavelengths used in our applications (figure A.2). The windows are slightly tilted, and the tilting angle is sufficient to observe several reflected beams (corresponding to reflections at the different interfaces) but small enough to be neglected. As a consequence, the cell can be theoretically approximated as a Fabry-Pérot (FP) interferometer, as described in Chapter 2. It is quite simple to show that using nanocells allows to obtain sub-Doppler spectral resolution. If we consider a laser beam of diameter $D = 1 \text{ mm}$, the time of flight (time from one cell wall to another) of atoms flying orthogonally to the laser radiation is $t_D = D/v$, where v is the speed of the atom (we will take 300 m.s^{-1} as a realistic example). This time of flight is roughly equal to $3 \mu\text{s}$. However, atoms flying along the laser beam (a few hundred nanometers) experience a time of flight $t_L = L/v$ several orders of magnitude smaller than t_D . The typical interaction time of a two level system being of the order of a few tens of nanoseconds, only the atoms flying orthogonally to the laser radiation have time to interact and contribute in the absorption, reflection and fluorescence signals. For these atoms, we have $\mathbf{k} \cdot \mathbf{v} = 0$, thus the resonances do not experience any Doppler shift Δ_D . Moreover, the efficiency of the optical pumping process inside the cell [31] given by

$$\eta = \frac{\Omega^2 \gamma t}{(\Delta + \mathbf{k} \cdot \mathbf{v})^2 + \Gamma_{tot}} \quad (1.9)$$

where Ω is the Rabi frequency, γ is the natural linewidth as presented in table A.1 and Γ_{tot} is the sum of all homogeneous and inhomogenous broadenings), is maximum when $\Delta = 0$ for $\mathbf{k} \cdot \mathbf{v} = 0$.

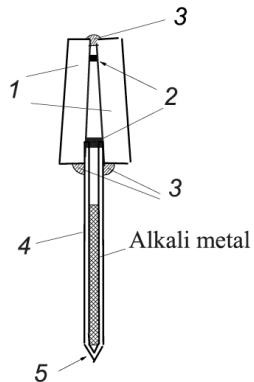


Figure 1.3: Typical scheme of a nanocell. 1: garnet or sapphire windows. 2: platinum or titanium strips. 3: high-temperature glue. 4: sapphire tube. 5: glass side-arm.



Figure 1.4: Picture of a nanocell. The interference profile arises from the reflection of the visible light on the internal surface of the cell and is shown by the black arrow. This pattern is one of the methods used to determine the cell thickness, but one can refer to [22] for a more precise description.

Chapter 2

Spectroscopy of nanometric-thin alkali vapors

2.1 Theoretical model

The theoretical model presented in this section has been proposed by Dutier *et al.* in [32]. In this model, a thin layer of atomic vapor is surrounded by two parallel dielectric windows of refractive indices n_1 and n_2 . Any effects that could be caused by the windows such as scattering and absorption, as well as birefringence and diffraction are neglected.

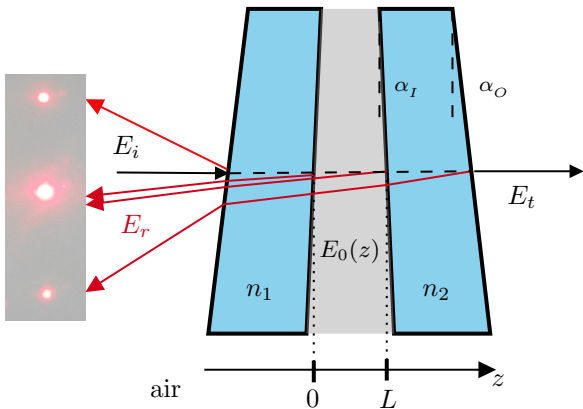


Figure 2.1: Scheme of a nanocell of thickness L with the incident, reflected and transmitted fields. The reflected field E_r takes into account reflections from air-air, window-vapor, vapor-window and window-air interfaces. α are the tilting angles of the windows.

The nanocell is illuminated under normal incidence (z -direction) by an incident field of wavevector \mathbf{k} and angular frequency ω

$$\mathbf{E}_i(z, t) = \frac{1}{2} E_i \exp[-i(\omega t - kn_1 z)] \cdot \mathbf{i} + c.c., \quad (2.1)$$

where \mathbf{i} stands for an arbitrary polarization. The goal of this problem is to express the reflected and transmitted fields, of general form

$$\mathbf{E}_r(z, t) = \frac{1}{2} E_r \exp[-i(\omega t + kn_1 z)] \cdot \mathbf{i} + c.c. \quad (2.2)$$

$$\mathbf{E}_t(z, t) = \frac{1}{2} E_t \exp[-i(\omega t - kn_2 z + \phi)] \cdot \mathbf{i} + c.c. \quad (2.3)$$

To do so, we will use the continuity equations for the fields at each interface, completed by the Maxwell equations describing the propagation of the fields in the atomic medium. It is important to note that this discussion is valid only in the dilute medium approximation, where the refractive index of the vapor can be neglected. The electric field \mathbf{E}_0 and the polarization \mathbf{P}_0 of the medium are formally written

$$\mathbf{E}_0(z, t) = \frac{1}{2} E_0(z) \exp[-i(\omega t - kz)] \cdot \mathbf{i} + c.c. \quad (2.4)$$

$$\mathbf{P}_0(z, t) = \frac{1}{2} P_0(z) \exp[-i(\omega t - kz)] \cdot \mathbf{i} + c.c., \quad (2.5)$$

where no assumptions are made on the form of the amplitudes $E_0(z)$ and $P_0(z)$ as inhomogeneities could occur along the z -direction, either arising from transient effects linked with atomic motion, or from nonlinear response of the medium. Under stationary cw excitation when the conductivity losses of the atomic medium are neglected, $E_0(z)$ and

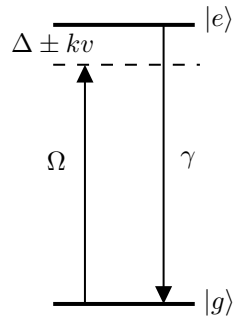


Figure 2.2: Two level system of Rabi frequency Ω and linewidth γ . $\Delta = \omega - \omega_0$ is the laser detuning with respect to the resonant frequency ω_0 .

the atomic response $P_0(z)$ obey the Maxwell propagation equations which reduce to

$$\frac{\partial^2}{\partial z^2} E_0(z) + 2ik \frac{\partial}{\partial z} E_0(z) = - \left(\frac{k^2}{\epsilon_0} \right) P_0(z). \quad (2.6)$$

Taking into account the electromagnetic continuity at $z = 0$ and $z = L$, one obtains the following system

$$E_i + E_r = E_0(0) \quad (2.7)$$

$$in_1 k(E_i - E_r) = ikE_0(0) + \frac{\partial}{\partial z} E_0(0) \quad (2.8)$$

$$E_0(L) = E_t \quad (2.9)$$

$$ikE_0(L) + \frac{\partial}{\partial z} E_0(L) = in_2 k E_t \quad (2.10)$$

one can show that equation (2.6) can be rewritten

$$\frac{\partial}{\partial z} E_0(L) - \frac{\partial}{\partial z} E_0(0) + 2ik[E_0(L) - E_0(0)] = 2ikI_f \quad (2.11)$$

$$\frac{\partial}{\partial z} E_0(L) \exp(2ikL) - \frac{\partial}{\partial z} E_0(0) = 2ikI_b, \quad (2.12)$$

where I_f (resp. I_b) is the forward (resp. backward) integral of the atomic response defined by

$$I_f = \frac{ik}{2\epsilon_0} \int_0^L P_0(z) dz \quad I_b = \frac{ik}{2\epsilon_0} \int_0^L P_0(z) \exp(2ikz) dz. \quad (2.13)$$

Solving the system of equations (2.7)-(2.12) allows to express the reflected and transmitted amplitudes as a sum of a resonant contributions (E_t'' , E_r'') and an empty-FP solution (E_t' , E_r'):

$$E_t = t_{02}t_{10}E_i/F + t_{02}(I_f - r_1I_b)/F = E_t' + E_t'' \quad (2.14)$$

$$E_r = (r_1 - r_2 \exp(2ikL))E_i/F + t_{01}(I_b - r_2I_f \exp(2ikL))/F = E_r' + E_r'', \quad (2.15)$$

where $F = 1 - r_1r_2 \exp(2ikL)$ is the quality factor of the cavity and

$$r_i = \frac{n_i - 1}{n_i + 1} \quad t_{0i} = \frac{2}{n_i + 1} \quad t_{10} = \frac{2n_1}{n_1 + 1}. \quad (2.16)$$

And one can finally show that the resonant amplitudes $S_t = |E_t|^2 - |E_t'|^2$ and $S_r = |E_r|^2 - |E_r'|^2$ (that can be interpreted as homodyne beatings with the transmitted (resp. reflected) field of an empty-FP cavity) corresponding to the observed transmitted and reflected signals read

$$S_t \approx 2t_{10}t_{02}E_i \operatorname{Re}(I_f - r_1I_b)/|F|^2 \quad (2.17)$$

$$S_r = 2t_{01}E_i \operatorname{Re}\{|[r_1 - r_2 \exp(-2ikL)] \times [I_b - r_2I_f \exp(2ikL)]|\}/|F|^2. \quad (2.18)$$

Consequently, we need to express the induced polarization $P_0(z)$ inside the vapor (viewed as an ensemble of identical two-level systems) in order to compute the transmitted (2.17) and reflected (2.18) signals. This can be done by different means, notably by building the density matrix of the system. However, in the limit of an optically thin vapor and due to the relatively weak incident field power usually used in the experiments, one can consider that the interaction regime is linear. The main lines of this approximation are provided in Appendix B.

In figures 2.3 and 2.4, we present the theoretical transmission and selective reflection (SR) lineshapes obtained with this model for an arbitrary two-level system, computed for a cell made of two identical windows $n_1 = n_2$ without antireflection coating.

The transmission lineshape greatly differs from what was predicted in [33]. This is due to the interferometric combination of the responses, as described by (B.1) and (B.2). The transmission (resp. absorption) spectrum thus includes a dispersive (resp. transmitted) contribution. An important thing to note is that even if the spectra clearly exhibit sub-Doppler features (the FWHM of the lineshapes are a few orders of magnitude smaller than the homogeneous linewidth of the system), one can observe additional narrowing of the transmission lineshape for $L = (2p+1)\lambda/2$, $p \in \mathbb{N}$. This phenomenon was first observed in the microwave domain [34] and is called coherent Dicke narrowing. As a manifestation of the FP nature of the cell, the SR signal vanishes for $L = p\lambda/2$. This was predicted by (2.18) in the case of two identical windows. Let us note that in this model, the linewidth of the system is a free parameter that can be fitted to the experimental measurements, as discussed in Appendix B. Moreover, the impact of the temperature is not properly reflected on the lineshapes obtained with this model. One only observes an increase of the signal amplitude with the number density N_D (eq. (B.8)). One would expect to observe broadening due to the increase of the number of atom-atom and atom-surface collisions with the temperature. In the last chapter, this model will be extended to the description of Zeeman spectra when applying an external magnetic field to the atomic vapor.

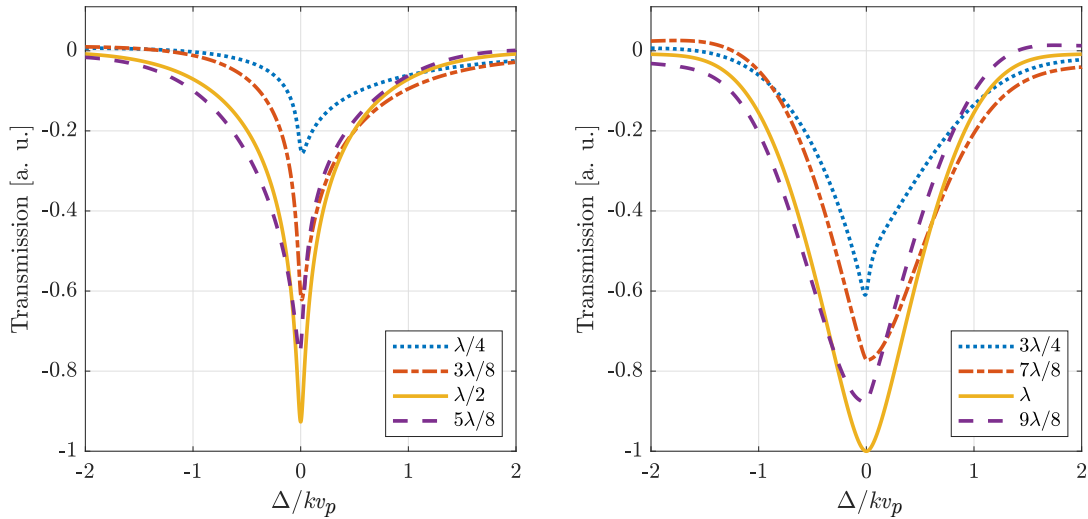


Figure 2.3: Theoretical transmission lineshape of an arbitrary two-level medium for two identical sapphire windows $r_1 = r_2 \approx 0.28$, and $\gamma/kv_p \approx 0.025$, where v_p is the most probable velocity. Left panel: the cell thickness L varies from $\lambda/4$ to $5\lambda/8$ with a step of $\lambda/8$. Right panel: the cell thickness L varies from $3\lambda/4$ to $9\lambda/8$ with a step of $\lambda/8$.

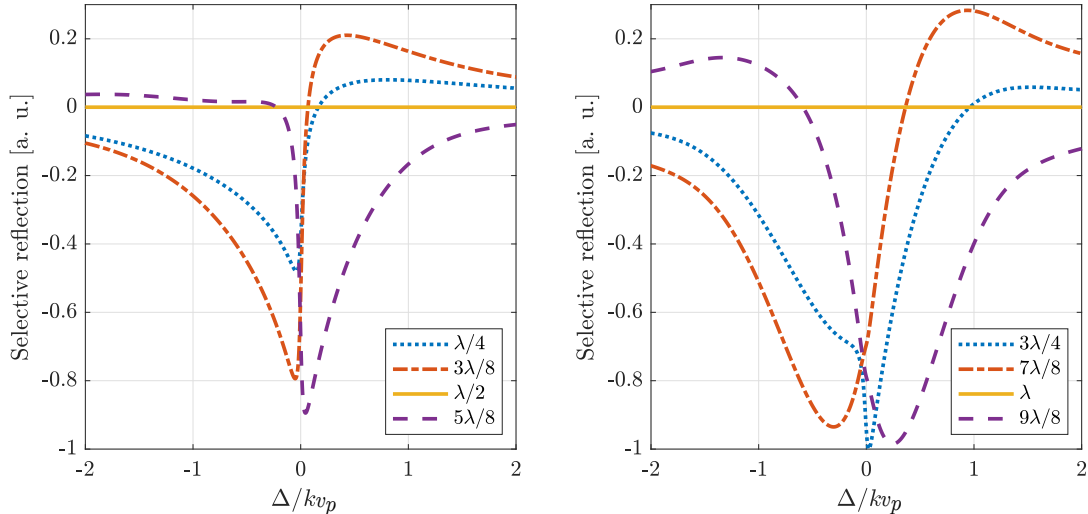


Figure 2.4: Theoretical reflection lineshape of an arbitrary two-level medium for two identical sapphire windows $r_1 = r_2 \approx 0.28$, and $\gamma/kv_p \approx 0.025$, where v_p is the most probable velocity. Left panel: the cell thickness L varies from $\lambda/4$ to $5\lambda/8$ with a step of $\lambda/8$. Right panel: the cell thickness L varies from $3\lambda/4$ to $9\lambda/8$ with a step of $\lambda/8$.

2.2 Sub-Doppler spectroscopy of a 400 nm-thick cesium vapor at room temperature

This theoretical model allowed us to compute absorption spectra of a cesium vapor and compare them with experimental spectra recorded at room temperature. This helped us visualize very efficiently the line broadening induced by the incident laser power (power broadening). The results have recently been submitted:

- A. Sargsyan, R. Momier, A. Papoyan and D. Sarkisyan, "Sub-Doppler spectroscopy of a 400 nm Cs atomic vapor column at room temperature", submitted to *J. Exp. Theor. Phys.*

Since the preprint is currently under review, we will not present the results here. We will now focus on the main of this work: the influence of the magnetic field on the alkali vapor, and study all the Zeeman transitions of the D lines of sodium.

Chapter 3

Influence of an external magnetic field

3.1 Theoretical model

The starting point of the theoretical model used for the description of alkali atoms in an electromagnetic field is the Dirac equation. For an electron of mass m and charge $-e$, this equation developed at the order v^2/c^2 reads

$$\left[\frac{1}{2m} \left(\mathbf{p} + \frac{e}{c} \mathbf{A} \right)^2 + \frac{e}{mc} \mathbf{S} \cdot (\nabla \times \mathbf{A}) - \frac{p^4}{8m^2 c^2} - \frac{e\hbar}{8m^2 c^2} \Delta V - \frac{e}{2m^2 c^2} \mathbf{S} \cdot (\nabla V \times \mathbf{p}) - eV \right] \Psi = E' \Psi, \quad (3.1)$$

where p is the magnitude of the electron's generalized momentum, and \mathbf{S} its spin momentum. This equation is valid in the usual gauge (\mathbf{A}, V) with \mathbf{A} the electromagnetic vector potential and V the scalar potential, such that

$$\mathbf{E} = -\frac{\partial \mathbf{A}}{\partial t} - \nabla V \quad \mathbf{B} = \nabla \times \mathbf{A}. \quad (3.2)$$

This equation involves many different terms:

- $\frac{1}{2m} (\mathbf{p} + \frac{e}{c} \mathbf{A})^2$ described the kinetic energy and interaction of the particle with the field of potential vector \mathbf{A} .
- $\frac{p^4}{8m^2 c^2}$ is the first order relativistic correction of the kinetic energy.
- $\frac{e}{mc} \mathbf{S} \cdot (\nabla \times \mathbf{A})$ is the interaction of the spin magnetic moment with the magnetic field $\mathbf{B} = \nabla \times \mathbf{A}$.
- $\frac{e}{2m^2 c^2} \mathbf{S} \cdot (\nabla V \times \mathbf{p})$ is the spin-orbit coupling term.
- $\frac{e\hbar}{8m^2 c^2} \Delta V$ is known as the Darwin term and produces an energy shift of the S -states.

All calculations are tractable in the case of alkali atoms (zero field Hamiltonian, spin-orbit Hamiltonian, Darwin term...). Here, we will only focus on the magnetic part of the Hamiltonian since we are interested in describing transitions between Zeeman sublevels arising from the influence of a static uniform magnetic field \mathbf{B} . In what follows, we derive the theoretical model presented in [18] and apply it to the case of a sodium vapor.

The general form of the magnetic contribution of the Hamiltonian \mathcal{H}_m is derived from equation (3.1) when the potential vector \mathbf{A} is non-zero. It reads

$$\mathcal{H}_m = \frac{e}{2mc} (\mathbf{p} \cdot \mathbf{A} + \mathbf{A} \cdot \mathbf{p}) + \frac{e}{mc} \mathbf{S} \cdot (\nabla \times \mathbf{A}). \quad (3.3)$$

We consider the case of a static magnetic field. Due to the small thickness of the nanocell, one can also safely consider the magnetic field to be uniform, that is

$$\mathbf{B} = \frac{1}{2} \nabla \times (\mathbf{B} \times \mathbf{r}) \quad \text{and} \quad \mathbf{A} = \frac{1}{2} (\mathbf{B} \times \mathbf{r}). \quad (3.4)$$

Taking into account that $[\mathbf{A}, \mathbf{r}] = 0$, \mathcal{H}_m takes the form

$$\mathcal{H}_m = \frac{\mu_B}{\hbar} \mathbf{B} \cdot (\mathbf{L} + 2\mathbf{S}) = \frac{\mu_B}{\hbar} B_z (g_L L_z + g_S S_z), \quad (3.5)$$

where $\mu_B = e\hbar/2mc$ is the Bohr magneton ($\mu_B \approx 1.333 \times 10^{10}$ MHz/T [35]). In (3.5), we chose z as the quantization axes for the momenta, and the magnetic field is also applied in the z -direction (ie. parallel to the laser). The factors g_L and g_S are respectively the orbital and spin Landé factors of the electron. While here the theory predicts $g_L = 1$ and $g_S = 2$, one can refer to table A.1 for the precise values (which differ due to corrections from QED [36]). It is worth noting that Dirac's theory does account for the spin-orbit interaction (total electronic angular momentum \mathbf{J}) but not for the coupling between \mathbf{J} and the intrinsic spin nuclear momentum \mathbf{I} . To solve this problem, one simply considers that the $\mathbf{J} - \mathbf{I}$ coupling adds a term $g_I I_z$ in equation (3.6), that is

$$\mathcal{H}_m = \frac{\mu_B}{\hbar} B_z (g_L L_z + g_S S_z + g_I I_z), \quad (3.6)$$

where g_I is called the nuclear Landé factor. Under the influence of the magnetic field, each hyperfine state F (Chapter 1) will split into $2F + 1$ Zeeman sublevels indexed by the pair of quantum numbers $|F, m_F\rangle$ ($-F \leq m_F \leq F$). By

writing \mathbf{L} , \mathbf{S} and \mathbf{I} as irreducible tensor operators and using the Wigner-Eckart theorem [37–39], one can express the Hamiltonian $\mathcal{H} = \mathcal{H}_0 + \mathcal{H}_m$ (zero-field + magnetic contribution) in the $|F, m_F\rangle$ basis. The matrix elements of \mathcal{H} obey the two following relations:

$$\langle F, m_F | \mathcal{H} | F, m_F \rangle = E_0(F) + \mu_B g_F m_F B_z \quad (3.7)$$

$$\langle F - 1 | \mathcal{H} | F, m_F \rangle = \frac{\mu_B B_z}{2} (g_J - g_I) \left(\frac{[(J+I+1)^2 - F^2][F^2 - (J-I)^2]}{F} \right)^{1/2} \left(\frac{F^2 - m_F^2}{F(2F+1)(2F-1)} \right)^{1/2}. \quad (3.8)$$

Equation (3.7) gives the diagonal terms of the Hamiltonian, which depend on the magnetic field B_z , the zero-field energy $E_0(F)$ of the associated F state (figure A.1) and the total atomic Landé factor g_F . The non-diagonal terms given by (3.8) are non-zero only if they respect the selection rules $\Delta F = \pm 1$, $\Delta m_F = 0$. As a result, \mathcal{H} is a block-diagonal matrix, each block corresponding to a given value of m_F . It is important to note that the sign convention in this model is different than in [18]. To obtain the same results, we must consider that the Bohr magneton is negative, and one can refer to [6] for further details. The Landé factors g_J and g_F are obtained with the following relations:

$$g_J = g_S \frac{J(J+1) + S(S+1) - L(L+1)}{2J(J+1)} + g_L \frac{J(J+1) - S(S+1) + L(L+1)}{2J(J+1)} \quad (3.9)$$

$$g_F = g_J \frac{F(F+1) - I(I+1) + J(J+1)}{2F(F+1)} + g_I \frac{F(F+1) + I(I+1) - J(J+1)}{2F(F+1)}. \quad (3.10)$$

By diagonalizing the Hamiltonian matrix for each value of the magnetic field, one obtains the eigenvalues which correspond to the energy of each Zeeman sublevel $|F, m_F\rangle$. In the small magnetic field limit ($B_z \ll B_0 = A_{n^2 S_{1/2}} \mu_B^{-1}$), the coupled basis $|F, m_F\rangle$ is a so-called "good" basis and the Zeeman sublevels split linearly according to relation (3.7). For $B_z \gg B_0$, it is best to describe the states in the uncoupled basis $|J, m_J, I, m_I\rangle$, where m_J and m_I are the quantum numbers associated to \mathbf{J} and \mathbf{I} , see for example [40]. In intermediate field ($B_z \simeq B_0$), one can obtain the energies of the ground states by using the Breit-Rabi formula, as presented in [41]. The new state vectors (eigenvectors of \mathcal{H} arising due to the influence of the magnetic field) are denoted by $|\Psi(F, m_F)\rangle$. They can be expressed as linear combinations of the set of unperturbed state vectors:

$$|\Psi(F, m_F)\rangle = \sum_{F'} \alpha_{F, F'}(B_z) |F', m_F\rangle. \quad (3.11)$$

Equation (3.11) is valid for both ground (denoted by the index g below) and excited states (denoted by the index e below). The coefficients $\alpha_{F, F'}(B_z)$ are the magnetic-field-dependent mixing coefficient reflecting the coupling of the Zeeman energy levels due to the magnetic field. It can be shown that the intensity A_{eg} of a transitions between two Zeeman sublevels $|\Psi(F_g, m_{F_g})\rangle$ and $|\Psi(F_e, m_{F_e})\rangle$ is proportional to the squared of the so-called "modified transfer coefficients". These coefficients are given by:

$$A_{eg} \propto a^2[|\Psi(F_e, m_{F_e})\rangle; |\Psi(F_g, m_{F_g})\rangle; q] = \left(\sum_{F'_e, F'_g} \alpha_{F_e, F'_e} a(F'_e, m_{F_e}; F'_g, m_{F_g}; q) \alpha_{F_g, F'_g} \right)^2, \quad (3.12)$$

where $a(F_e, m_{F_e}; F_g, m_{F_g}; q)$ are the so-called unperturbed transfer coefficients given by

$$a(F_e, m_{F_e}; F_g, m_{F_g}; q) = (-1)^{1+I+J_e+F_e+F_g-m_{F_e}} \times \sqrt{2F_e+1} \sqrt{2F_g+1} \sqrt{2J_e+1} \begin{pmatrix} F_e & 1 & F_g \\ -m_{F_e} & q & m_{F_g} \end{pmatrix} \left\{ \begin{matrix} F_e & 1 & F_g \\ J_g & I & J_e \end{matrix} \right\}. \quad (3.13)$$

In relation (3.13), the parenthesis represent a Wigner 3j-symbol and the curly brackets a 6j-symbol. The index q reflects the polarization of the laser radiation, $q = 0, \pm 1$ for π, σ^\pm . The model allows to study each individual Zeeman transition of the D_1 and D_2 lines of any alkali atom, but is also valid for other lines with similar structures, as presented in [42]. As a last remark, in this work all transitions will be labelled in the basis $|F, m_F\rangle$ for convenience. The transition frequencies ω_{eg} are simply obtained by:

$$\omega_{eg}(B) = \omega_e - \omega_g, \quad (3.14)$$

where $\omega_{e,g}$ are the eigenvalues of the Hamiltonian, here obtained by numerical diagonalization. In figures 3.1 and 3.2 are plotted the eigenvalues of the Hamiltonian of sodium ground ($3^2 S_{1/2}$) state and D_2 excited ($3^2 P_{3/2}$) state. In the low magnetic field limit, the levels are grouped by values of F , and they are grouped by value of m_J for strong magnetic fields.

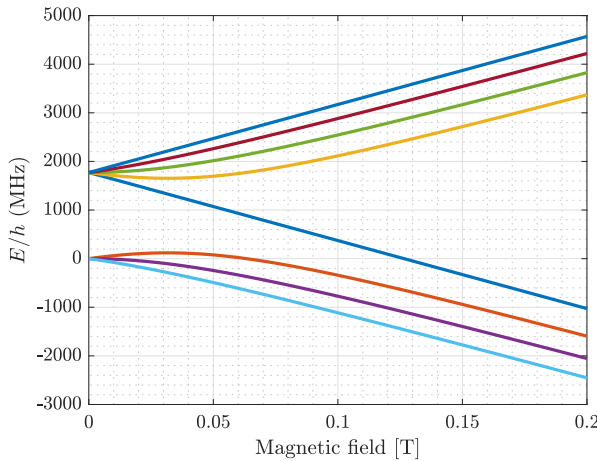


Figure 3.1: Sodium ground ($3^2S_{1/2}$) state Zeeman structure as a function of the magnetic field. The magnetic field range is restricted up to 0.2T for clarity.

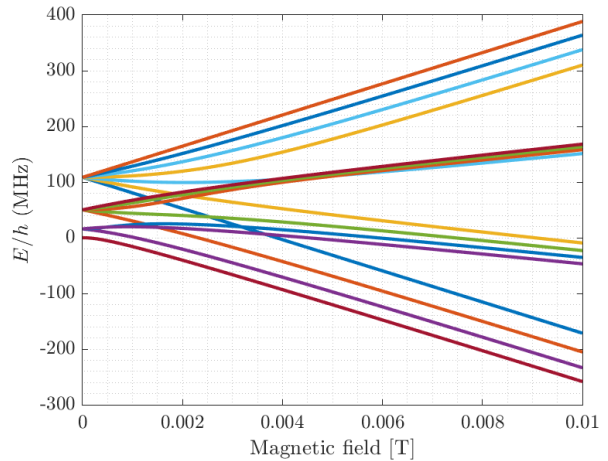


Figure 3.2: Sodium D_2 excited ($3^2P_{3/2}$) Zeeman structure as a function of the magnetic field. The magnetic field range is restricted up to 0.01T for clarity.

The theoretical model presented in Chapter 2 can be extended to the case of an atomic vapor under the influence of a magnetic field. To do so, we consider that the vapor is an ensemble of two-level systems with different resonant frequencies describing the different Zeeman transitions. In this case, the transmitted and reflected intensities (in the linear interaction regime) are rewritten

$$I_T^{lin} = \sum_i C_i \int_{-\infty}^{+\infty} W(v)g(\Delta_i, v, L)dv \quad (3.15)$$

$$I_{SR}^{lin} = \sum_i C_i \int_{-\infty}^{+\infty} W(v)h_{\pm}(\Delta_i, v, L)dv, \quad (3.16)$$

where $\Delta = \omega - \omega_i$ is the laser detuning with each Zeeman transition having a resonant frequency ω_i obtained with equation (3.14). The amplitude C_i obtained with equation (B.8) mainly depends on the transition dipole moment, computed with equation (3.12).

3.2 Sub-Doppler spectra of sodium D lines in a wide range of magnetic field

This theoretical model, combined with the one presented in Chapter 2, led to the following article, accepted for publication on June 1st, 2021 in Journal of Quantitative Spectroscopy and Radiative Transfer:

- R. Momier, A. Papoyan and C. Leroy, "Sub-Doppler spectra of sodium D lines in a wide range of magnetic field: theoretical study", accepted by *J. Quant. Spectrosc. Radiat. Transf.* (June 1st, 2021), arXiv:2104.14896.

A thorough description of the behavior of both D_1 and D_2 lines of sodium within a magnetic field is provided. The article is presented hereafter.

Sub-Doppler spectra of sodium D lines in a wide range of magnetic field: theoretical study

Rodolphe MOMIER^{a,b}, Aram V. PAPOYAN^b, Claude LEROY^{a,*}

^aLaboratoire Interdisciplinaire Carnot de Bourgogne, UMR CNRS 6303, Université Bourgogne Franche-Comté, 21000 Dijon, France

^bInstitute for Physical Research, NAS of Armenia, Ashtarak-2, 0203, Republic of Armenia

Abstract

We compute the interaction of a sodium vapor with a static magnetic field ranging from 0 up to 1 Tesla, which allows to obtain the behavior of all Zeeman transitions as a function of the magnetic field for any polarization of incident laser radiation: π, σ^\pm . We use these results combined with a Fabry-Pérot microcavity model to describe the transmitted and reflected signal of a sodium vapor confined in a nanometric-thin cell. This allows us to present for the first time high resolution absorption spectra, and provide a complete description of the Zeeman transitions, along with some important peculiarities such as the appearance of guiding transitions and magnetically-induced circular dichroism. The obtained theoretical results can be used in the upcoming experiments with sodium vapor nanocells.

Keywords: Sub-Doppler spectroscopy, Sodium, Alkali metal vapor, Zeeman effect, Magneto-optical processes

1. Introduction

Alkali metal atoms are recognized as classical objects of research in atomic physics for a number of reasons. In terms of experiment, their convenience is due to the high density of atomic vapor at relatively low temperatures, and the presence of strong optical transitions from the ground state (D_1 and D_2 lines) in the visible or near-infrared region of the spectrum. From a theoretical point of view, they are attractive due to simplicity of their energy levels caused by the presence of a single electron on the outermost shell, which significantly facilitates the calculations, so that spectroscopic data are now very well documented [1–7].

Magneto-optical phenomena in alkali metal vapors are of particular interest. Complete understanding of various magneto-optical effects occurring in alkali vapors [8] is important since they are widely used, for example in fundamental and applied studies of electromagnetically induced transparency [9, 10], Faraday filters [11, 12], optical magnetometry [13], laser-frequency locking [14] and elsewhere. Such phenomena often rely on the peculiarities of the behavior of Zeeman transitions, so that frequency separation of individual transitions is of high importance. Meanwhile for a vapor media, the thermal motion of atoms resulting in Doppler broadening leads to overlapping of hyperfine transitions and their Zeeman components, thus limiting its spectroscopic applicability.

Significant sub-Doppler narrowing of atomic transitions can be attained with the use of so-called optical nanocells [15–17]. Being enclosed in optical cells with a thickness commensurable with the resonant wavelength, alkali metal vapors become a powerful tool for the high-resolution atomic spectroscopy, opening new possibilities for studying magneto-optical pro-

cesses, where spectral resolution of individual transitions between magnetic sublevels (Zeeman transitions) is essential. Complete determination of the behavior of all the possible individual Zeeman transitions can be done using a well-known theoretical model first provided by Tremblay *et al.* [18]. Importantly, besides frequency splitting in magnetic field, Zeeman transitions undergo also significant probability changes [17]. This allows to observe the appearance of several peculiarities, such as Guiding Transitions (GT) and two different types of so-called Magnetically-induced Circular Dichroism (MCD) [19, 20]. Moreover, several efficient techniques have been developed to enhance a spectral visibility of Zeeman transitions while preserving their relative probability scaling, such as derivative of Selective Reflection (dSR) [13, 21] and Second Derivative of absorption (SD) [22–24].

Most of the experimental studies were done using rubidium and cesium atomic vapor due to the availability of relatively inexpensive cw diode lasers operating in their resonant wavelength range. For these atoms, also the hyperfine splitting is affordably large (the lowest frequency separation between adjacent upper states is ≈ 30 MHz for ^{85}Rb). The magneto-optical effects on sodium D_1 and D_2 lines have been much less studied. The reason for this is the lack of convenient inexpensive lasers operating in the region of these resonances (589.6 nm and 589.0 nm, respectively), as well as the relatively low vapor density. Although some information concerning Zeeman transitions of sodium exist in the literature [25–27], the available information is far from being complete. Meanwhile, recently interest in magneto-optical processes in sodium vapor has increased, in particular, due to the topical problem of mesospheric sodium [28].

In this paper, we provide for the first time a comprehensive set of theoretical sub-Doppler spectra of all Zeeman transitions for both lines of sodium in a magnetic field, as well as a thor-

*Corresponding author: claude.leroy@u-bourgogne.fr

ough description of most of the peculiarities that occur. The results we present throughout this paper are qualitatively analogous to the ones obtained for the D_1 and D_2 line of ^{87}Rb and ^{39}K representing similar quantum systems, therefore we expect total agreement between them and upcoming experiments with Na nanocells.

2. Theoretical model

2.1. Interaction of an alkali vapor with a transverse magnetic field

The Hamiltonian matrix of alkali atoms interacting with a static magnetic field is expressed as

$$\mathcal{H} = \mathcal{H}_0 + \mathcal{H}_m \quad (1)$$

where \mathcal{H}_0 is the unperturbed (zero-field) Hamiltonian and \mathcal{H}_m is the magnetic interaction contribution given by

$$\mathcal{H}_m = -\frac{\mu_B B_z}{\hbar} (g_L L_z + g_S S_z + g_I I_z). \quad (2)$$

In relation (2), μ_B is the Bohr magneton, g_L , g_S and g_I are respectively the orbital, spin and nuclear Landé factors. L_z , S_z and I_z are the projections of the orbital, spin and nuclear angular momenta along the magnetic field direction z . Due to the influence of the magnetic field, the hyperfine energy levels F split into Zeeman sublevels denoted $|F, m_F\rangle$ in the coupled basis, with m_F the magnetic quantum number varying from $-F$ to $+F$. As it has been developed in [18], the matrix elements of \mathcal{H} obey the two following relations:

$$\langle F, m_F | \mathcal{H} | F, m_F \rangle = E_0(F) - \mu_B g_F m_F B_z \quad (3)$$

$$\begin{aligned} \langle F-1, m_F | \mathcal{H} | F, m_F \rangle &= \langle F, m_F | \mathcal{H} | F-1, m_F \rangle \\ &= -\frac{\mu_B B_z}{2} (g_J - g_I) \left(\frac{[(J+I+1)^2 - F^2][F^2 - (J-I)^2]}{F} \right)^{1/2} \\ &\times \left(\frac{F^2 - m_F^2}{F(2F+1)(2F-1)} \right)^{1/2}. \end{aligned} \quad (4)$$

Equation (3) gives the diagonal terms of the Hamiltonian, which depend on the projection B_z of \vec{B} , the zero-field energy $E_0(F)$ of the F level and the Landé factor g_F associated to the $|F, m_F\rangle$ sublevel (see for example [29] or [30] for a more detailed description). The non-diagonal terms, given by relation (4), are non-zero only if they respect the selection rules $\Delta F = \pm 1$, $\Delta m_F = 0$. As a result, the Hamiltonian \mathcal{H} is a block diagonal matrix, each block corresponding to a value of m_F . By diagonalizing the Hamiltonian matrix for each value of the magnetic field, one obtains the eigenvalues which correspond to the energy of each Zeeman sublevel $|F, m_F\rangle$. In the small magnetic field limit ($B_z \ll B_0 = A_{3^2S_{1/2}} \mu_B^{-1} \approx 63.3$ mT, where $A_{3^2S_{1/2}}$ is the magnetic dipole constant), the coupled basis is a so-called "good" basis, the Zeeman sublevels split linearly according to (3). For $B_z \gg B_0$, it is best to describe the states

μ_B/h	$1.39962449361(42) \times 10^{10}$ Hz/T
$A_{3^2S_{1/2}}$	885.8130644(5) MHz
g_S	2.00231930436256(35)
g_L	0.99997613
g_I	-0.0008046108(8)

Table 1: Numerical data to compute the interaction of the ^{23}Na vapor with a magnetic field.

in the uncoupled basis $|J, m_J, I, m_I\rangle$ where m_J and m_I are projections of the angular momentum J and nuclear momentum I , see for example [31]. In intermediate field ($B_z \simeq B_0$) one can obtain the energies of the ground states by using the Breit-Rabi formula, as presented in [32]. All the numerical data needed for the computations can be found in the literature, for example in [4], along with many other relevant parameters and constants. All values used for the physical constants are the ones recommended by NIST [33]. The necessary values are given in table 1. The new state vectors arising due to the influence of the magnetic field are denoted by $|\Psi(F, m_F)\rangle$. They can be expressed as linear combinations of the set of unperturbed state vectors:

$$|\Psi(F, m_F)\rangle = \sum_{F'} \alpha_{F,F'}(B) |F', m_F\rangle. \quad (5)$$

Relation (5) is valid for both ground (denoted by the index g below) and excited states (denoted by the index e below). $\alpha_{F,F'}(B)$ are the magnetic-field-dependent mixing coefficients reflecting the coupling of the Zeeman energy levels due to the magnetic field. The intensity A_{eg} of a transition between two Zeeman sublevels $|\Psi(F_g, m_{F_g})\rangle$ and $|\Psi(F_e, m_{F_e})\rangle$ is proportional to the squared of the so-called "modified transfer coefficients". These coefficients are given by

$$\begin{aligned} A_{eg} &\propto a^2[|\Psi(F_e, m_{F_e})\rangle; |\Psi(F_g, m_{F_g})\rangle; q] \\ &= \left(\sum_{F'_e, F'_g} \alpha_{F_e, F'_e} a(F'_e, m_{F_e}; F'_g, m_{F_g}; q) \alpha_{F_g, F'_g} \right)^2 \end{aligned} \quad (6)$$

where $a(F_e, m_{F_e}; F_g, m_{F_g}; q)$ are the unperturbed transfer coefficients. They have the following form:

$$\begin{aligned} a(F_e, m_{F_e}; F_g, m_{F_g}; q) &= (-1)^{1+I+J_e+F_e+F_g-m_{F_e}} \sqrt{2F_e+1} \\ &\times \sqrt{2F_g+1} \sqrt{2J_e+1} \begin{pmatrix} F_e & 1 & F_g \\ -m_{F_e} & q & m_{F_g} \end{pmatrix} \begin{Bmatrix} F_e & 1 & F_g \\ J_g & I & J_e \end{Bmatrix}. \end{aligned} \quad (7)$$

In relation (7), parenthesis represent a Wigner 3j-symbol and curly brackets a 6j-symbol. The index q reflects the polarization of the laser radiation, $q = 0, \pm 1$ for π, σ^\pm . The model allows to study each individual Zeeman transition of the D_1 and D_2 lines of any alkali atom, but is also valid for other lines with similar structure, as presented in [34]. As a last remark, in this work all transitions will be labelled in the basis $|F, m_F\rangle$ for convenience although these quantum numbers form a "good" basis only for low magnetic fields.

2.2. Transmitted and reflected signal for a vapor of nanometric thickness

One of the possible ways to obtain sub-Doppler resolution during experiments is to use a nano- or micrometric thin-cell filled with an atomic vapor. Such experiments have been thoroughly described in [15, 16, 35–37]. In what follows, we recall briefly the theoretical model that can be used to compute the fields that are reflected S_r and transmitted S_t through a thin cavity (maximum a few wavelengths) seen as a Fabry-Pérot interferometer. The reader can refer to [38] for a complete description of the model. The transmitted and reflected signals containing the information on the atomic vapor have the following expressions

$$S_t \simeq 2t_{wc}t_{cw}^2 E_i \text{Re} \left\{ I_f - r_w I_b \right\} / |Q|^2 \quad (8)$$

$$\begin{aligned} S_r \simeq 2t_{cw}E_i \text{Re} \{ & r_w [1 - \exp(-2ikL)] \\ & \times [I_b - r_w I_f \exp(2ikL)] \} / |Q|^2, \end{aligned} \quad (9)$$

where r_w is the reflection coefficient and t_{cw} (resp. t_{wc}) is the transmission coefficient at the vapor-window interface (resp. window-vapor interface). $Q = 1 - r_w^2 \exp(2ikL)$ is the quality factor of the cavity of length L , and all possible losses due to the windows are neglected. I_f and I_b are called forward and backward integrals of the atomic response

$$I_f = I_T^{lin} - r_w I_{SR}^{lin} \quad (10)$$

$$I_b = I_{SR}^{lin} - r_w \exp(2ikL) I_T^{lin}, \quad (11)$$

where I_T^{lin} and I_{SR}^{lin} are the transmitted and reflected signals in the linear regime whose expressions are derived in [38]. The homogeneous linewidth of the transmitted signal $\gamma = \Gamma_{\text{nat}}/2$ is a free parameter which can be replaced by $\gamma = \Gamma_{\text{nat}}/2 + \gamma_f$ to account for additional decoherence processes (for example collisional broadening). This model, valid for a two-level system having a resonant frequency ω_0 , can be extended to an ensemble of two-level systems in order to describe each hyperfine transition having a resonant frequency $\omega_i = \omega_e - \omega_g$ and an amplitude depending mainly on the transition intensity A_{eg} , computed using relation (6) (see [30]). All absorption spectra presented in this paper will be computed for a cell thickness $\lambda/2$ (where λ is the resonant wavelength of the optical transition) and a linewidth of 100 MHz. This linewidth is chosen arbitrarily larger than for other alkalis due to the larger Doppler broadening of sodium D lines, as it will be discussed later in this paper. Experimentally, all studies are typically performed around this thickness due to the appearance of coherent Dicke narrowing (first observed in the microwave domain [39], and first presented in [40]). Narrowing of the resonance occurs periodically for $L = (2p+1)\lambda/2$ with $p \in \mathbb{N}$. Different lineshapes for the absorption and reflection signal are presented in [38, 40]. It is relevant to note that for other thicknesses, one obtains assymetric lineshapes arising from different dispersive contributions involved in the expressions of the transmitted and reflected fields. As an example of the results provided by this theoretical model, we present in figure 1 an absorption and dSR spectrum of D_2 line π -transitions for an external magnetic field $B_z = 50$ mT. The model predicts vanishing of the reflected signal for $L = (2p+1)\lambda/2$, thus

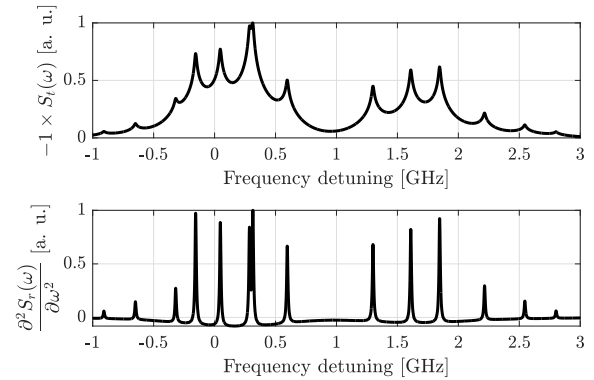


Figure 1: Sodium D_2 line spectra for π -polarized laser radiation. Top panel: absorption spectrum computed for $L = \lambda/2$. Bottom panel: dSR spectrum computed for $L = \lambda/2 - 30$ nm.

the dSR spectrum presented is computed for a slightly smaller thickness of $\lambda/2 - 30$ nm.

3. Sodium D_1 line

Sodium only has one stable isotope ^{23}Na with natural abundance of nearly 100%. The D_1 line corresponds to transitions occurring between the states $F_g = 1, 2$ of $3^2S_{1/2}$ and $F_e = 1, 2$ of $3^2P_{1/2}$. The Zeeman manifold is thus analogous to the one of ^{87}Rb or ^{39}K D_1 line. A π -polarized incident laser will excite 14 transitions, whereas left (or right) circularly polarized laser will excite only 12 transitions. In total for sodium D_1 line, 38 $|F_g, m_{F_g}\rangle \rightarrow |F_e, m_{F_e}\rangle$ Zeeman transitions are possible. A scheme depicting all of them is presented in figure 2. Throughout this work, the computations have been performed using $\zeta = 1.7716261288(10)$ GHz the hyperfine splitting between the two ground states $F_g = 1$ and $F_g = 2$. In the same manner, $\zeta' = 188.88(26)$ MHz is the hyperfine splitting between $F_e = 1$ and $F_e = 2$ [4].

3.1. Linearly polarized incident radiation

Let us first focus on π -transitions. As said before, in this case 14 transitions are possible. All these transitions are so-called "allowed" since they respect the selection rules on F : $\Delta F = 0, \pm 1$. The transition intensity is proportional to the square of the modified transfer coefficient. The results obtained for $a^2[|\Psi(F_e, m_{F_e})\rangle; |\Psi(F_g, m_{F_g})\rangle; 0]$ are presented in figure 3. For the sake of clarity to avoid overlapping, we separate the two following cases: transitions labelled 1 to 6 with ground state $F_g = 1$ are represented on panel a), and transitions labelled 7 to 14 with ground state $F_g = 2$ are represented on panel b). Several observations can be made from figure 3. The amplitudes of transitions 1, 3, 5 (see figure 3a), 7, 9, 11, 13 and 14 (see figure 3b) remain considerable for $B_z \gg B_0$, thus 8 transitions will remain present in the spectrum when the magnetic field is high enough. These transitions will be denoted as r-transitions, where r stands for remaining. Here, they obey the selection $\Delta F = 0$ at low magnetic field (F is not a good quantum number at high magnetic field), and $\Delta m_l = \Delta m_J = 0$ for

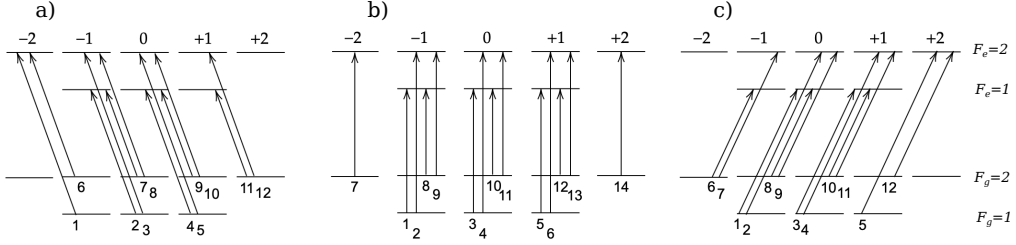


Figure 2: All possible Zeeman transitions for the D_1 line of ^{23}Na in the basis $|F, m_F\rangle$. a) σ^- -transitions, b) π -transitions, c) σ^+ -transitions.

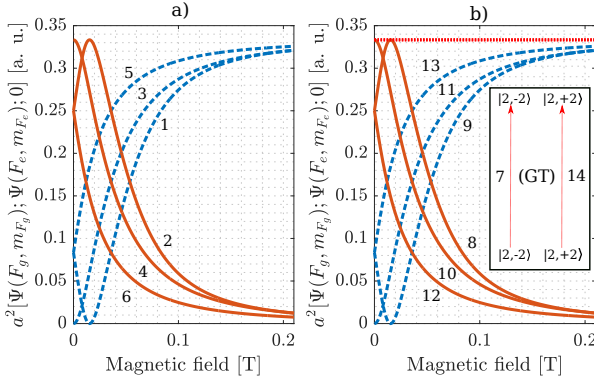


Figure 3: (color online) Sodium D_1 line hyperfine transition intensities for π -polarized laser radiation in arbitrary units. a) transitions from $F_g = 1$, b) transitions from $F_g = 2$. The guiding transitions 7 and 14 are represented in red (dotted lines). In blue (dashed lines), we represent the transitions whose intensities remain considerable past $B_0 \approx 63.3$ mT, as opposed to the orange curves (solid lines). Magnetic field varies up to 0.2 T here for clarity.

high magnetic field. The r-transitions 1, 3, 5 occur between $F_g = F_e = 1$, and the others between $F_g = F_e = 2$. Similarly, transitions 2, 4, 6, 8, 10 and 12 will be called v-transitions, where v stands for vanishing, since their amplitude becomes negligible for $B_z \gg B_0$. One can notice that some of the r-transitions show $a^2 \approx 0$ for low magnetic field and experience a huge amplitude growth as the magnetic field increases. For these reason, we call them Magnetically Induced (MI), although they are theoretically allowed by the selection rule $\Delta F = 0, \pm 1$. Another peculiarity is the appearance of “transition cancellations”, occurring here at around 15 mT. This value depends on the different hyperfine splittings. This phenomenon was already mentioned in [18] but no complete description was done. Precise discussion of these cancellations is out of the scope of this paper, however we have provided a thorough analysis and a way to determine precisely the magnetic field values leading to dipole moment cancellation in [34, 41, 42]. Using the relations provided in these works, we can determine that transitions 1 and 9 experience dipole moment cancellation for

$$B = \frac{1}{\mu_B} \frac{3\zeta\zeta'}{(3g_I - 4g_L + g_S)\zeta + 3(g_I - g_S)\zeta'} \approx 15.32 \text{ mT}. \quad (12)$$

The last peculiarity that appears is the presence of two r-transitions (7 and 14) having a constant amplitude throughout the whole range of magnetic field. These transitions occur between uncoupled states (following the definition of relation

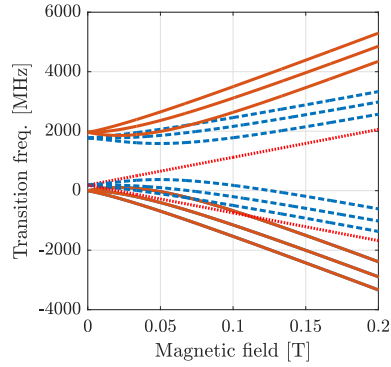


Figure 4: (color online) π -transition frequencies of sodium D_1 line as a function of the magnetic field. The color code corresponds to the one used in figure 3. The zero frequency is set to the transition $F_g = 1 \rightarrow F_e = 1$.

(5)): such states do not experience any mixing with their neighbors (with the same m_F value), thus leading to magnetic-field-independent transition amplitudes. As shown on the inset of the right panel of figure 3b, these transitions are called Guiding Transitions (GT). For further analysis, we present in figure 4 the frequencies $\omega_{eg}(B_z) = (E_e(B_z) - E_g(B_z))$ of all the possible π -transitions.

From figure 4, one can notice the following: the two guiding transitions (represented in red dotted lines) occur between uncoupled states having for only difference their m_F values ($m_{F_g} = m_{F_e} = \pm 2$), their frequency shifts are perfectly linear with respect to B_z and only differ by sign. Going back to the model of section 1, the uncoupled states give rise to 1×1 blocks in \mathcal{H} and thus their Zeeman splitting is perfectly described by relation (3), hence it is quite straightforward to show that their slope is

$$s_{\pm, GT}^{D_1^{(\pi)}} \approx \pm \frac{2\mu_B}{3}, \quad (13)$$

under the approximation $g_S \approx 2$, $g_L \approx 1$ and $g_I \ll g_J$. Numerically, by using the values provided in table 1, we obtain $s_{\pm, GT}^{D_1^{(\pi)}} = \pm 9.35269 \times 10^3$ MHz/T. Each group of r-transitions is thus driven by one of the GTs, more precisely r-transitions 1, 3 and 5 are driven by the GT labelled 7 having a slope $s_{-, GT}^{D_1^{(\pi)}} = -2\mu_B/3$, and r-transitions 9, 11 and 13 are driven by the GT labelled 14 having a slope $s_{+, GT}^{D_1^{(\pi)}} = 2\mu_B/3$, with μ_B chosen to be negative as mentioned earlier. Driven means here that each individual transition belonging to a given group is bounded in amplitude by the one the Guiding Transition, and all the frequency

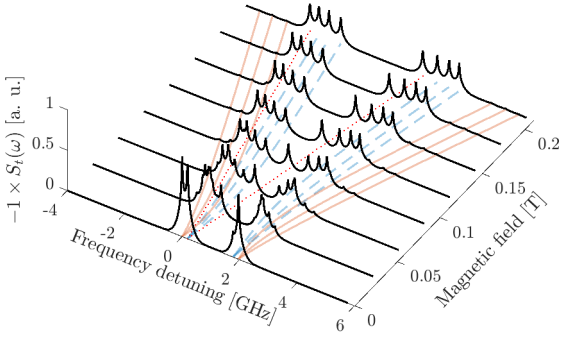


Figure 5: (color online) Absorption spectra of the D_1 line of sodium for π -polarized incident laser radiation. The magnetic field intensity varies from 0 to 0.21 T with a step of 30 mT. The shadow lines on the (x, y) plane are the same transition frequencies shown in figure 4. Each component has a Full Width at Half Maximum (FWHM) of $\omega_{\text{FWHM}} \approx 100$ MHz. The zero frequency is set to the transition $F_g = 1 \rightarrow F_e = 1$.

shifts asymptotically tend to a linear behavior when $B_z \gg B_0$ is high enough, with the slope being $s_{\pm,r}^{D_1^{(\pi)}} = s_{\pm,GT}^{D_1^{(\pi)}}$, as written in relation (13). Due to the absence of coupling between states, the modified transfer coefficient of a GT occurring between two uncoupled states $|F_g, m_{F_g}\rangle \rightarrow |F_e, m_{F_e}\rangle$ is exactly equal to the unperturbed transfer coefficient $a^2(F_e, m_{F_e}; F_g, m_{F_g}, q)$. For transitions 7 and 14, we obtain

$$a(2, \pm 2; 2, \pm 2; q=0) = \pm \frac{1}{\sqrt{3}} \Rightarrow a^2 = \frac{1}{3}. \quad (14)$$

Past B_0 , the 8 r-transitions remain in the spectrum, which is a manifestation of the hyperfine Paschen-Back regime. This behavior has been observed experimentally for cesium, rubidium and potassium (for example in [43]). As mentioned before, experimental results are harder to provide due to the lack of diode lasers operating in the wavelength range of sodium. However, a sodium nanocell is available [24]. A set of theoretical absorption spectra for all π -transitions of sodium D_1 line is presented in figure 5 for visualization.

All the previous statements are visible in figure 5. The r-transitions can be separated in two groups, all tending to the same amplitude and a complete symmetry between the red and blue wings of the spectrum appears when B_z is high enough. Although becoming invisible, the v-transition frequency shifts also exhibit a linear behavior at high magnetic fields, tending to a slope twice bigger than for the r-transitions. Precisely, $s_{\pm,v}^{D_1^{(\pi)}} = 2s_{\pm,r}^{D_1^{(\pi)}} \approx \pm 4\mu_B/3$ using the same approximations. It is usually estimated that complete Hyperfine Paschen-Back regime is reached when a magnetic field $B_z > 10B_0$ is applied. This corresponds here to a magnetic field $B_z \approx 0.63$ T. As a comparison, for ^{87}Rb , $B_0 \approx 0.24$ T [2] and for ^{133}Cs , $B_0 \approx 0.16$ T [3]. Theoretically, this makes sodium, as well as ^{39}K [6, 30] more convenient than cesium or rubidium for the experimental study of magnetic-optical processes occurring in the com-

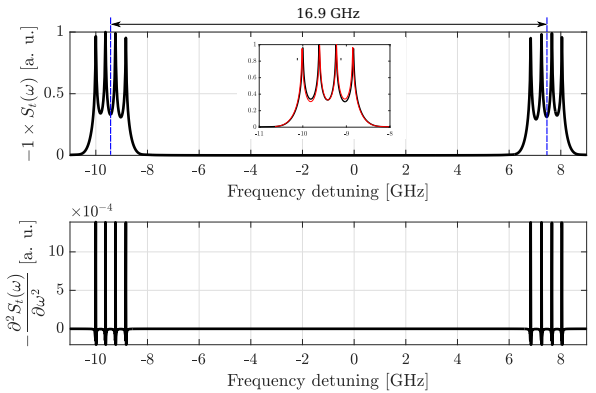


Figure 6: (color online) Top panel: absorption spectra of the D_1 line of sodium for π -polarized incident laser radiation in the hyperfine Paschen-Back regime ($B_z = 0.9$ T). Bottom panel: second derivative (SD). Inset: "mirror" overlap of the two groups when the high-frequency group is computed as a function of $-\omega$. The top curve has been normalized so that the maximum amplitude is 1.

plete hyperfine Paschen-Back since it is reached for a much weaker value of external magnetic field. However, since the natural linewidth of sodium D_1 line $\Gamma_{\text{nat}}/2\pi = 9.765$ MHz [4] is nearly twice bigger than for the D_1 lines of cesium or rubidium, one expects to obtain significantly broader lines when studying sodium. The linewidth is also affected by the inhomogeneous Doppler broadening Γ_D given by

$$\Gamma_D = \omega_0 \sqrt{\frac{8k_B T \ln 2}{mc^2}} \quad (15)$$

(see [44]), bigger for the D_1 line of sodium than in the case of rubidium or cesium. In relation (15), ω_0 is the central angular frequency of the transition, m is the atomic mass, T is the temperature of vapor, c is the speed of light and k_B is the Boltzmann constant. However, performing experiments with nanocells allows to reach sub-Doppler spectral resolution [15]. In figure 6, we present a theoretical absorption spectrum of sodium D_1 π -transitions, computed with the same numerical parameters as before, as long with the second derivative spectrum (SD).

Due to the linewidth $\omega_{\text{FWHM}} \approx 100$ MHz, even for a magnetic field $B_z \gg 10B_0$, the peaks are not totally resolved hence resulting in a variation of the peaks' amplitude. In the experiments, as demonstrated on the bottom panel of figure 6, SD would allow to obtain completely resolved peaks, all having the same amplitude. DSR would also be suitable here. These techniques allow to obtain much narrower resonances (two to three times, see [30]). One can also see that all the peaks are evenly spaced, which is a manifestation of the linear behavior of the frequency shifts mentioned above and a good sign HPB regime is reached. Moreover, as shown by the inset, the red and blue wings of the spectrum are completely symmetric. The frequency detuning $\Delta\omega_r^{D_1^{(\pi)}}$ between the two groups of 4 r-transitions (their centers of gravity, see the dashed blue lines in figure 6) for $B_z \gg B_0$ can be estimated roughly by performing the difference between the two GTs, thus

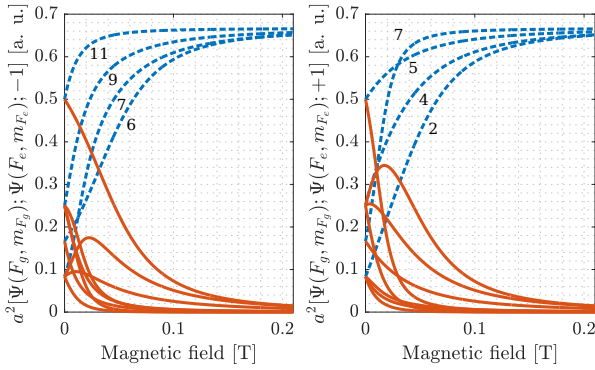


Figure 7: (color online) Sodium D_1 line Zeeman transition intensities for circularly polarized laser radiation. a) σ^- -transitions. b) σ^+ -transitions. Labelling is provided only for the non-vanishing transitions (dashed blue lines) and is the same as on panels a) and c) of figure 2.

$$\Delta\omega_r^{D_1^{(\pi)}} \approx \left| \frac{4\mu_B B_z}{3} \right|. \quad (16)$$

For a magnetic field $B_z = 0.9$ T, we obtain $\Delta\omega_r^{D_1^{(\pi)}} \approx 16.8$ GHz which is in excellent agreement with the value 16.9 GHz computed numerically and shown in figure 6.

3.2. Circularly polarized incident radiation

All the possible σ^- (resp. σ^+) transitions of the D_1 line of sodium are schematized on panel a) (resp. panel c)) of figure 2, and their associated intensities are presented in figure 7. As a first remark, no σ^\pm transition has a constant amplitude throughout the whole magnetic field range, which is due to the fact that no transition occurs between uncoupled states. At best, only the excited state is uncoupled (transitions 1 and 6 for σ^- , and their “symmetric” transitions 5 and 12 for σ^+), but this is not enough to avoid the magnetic-field dependence of the transition intensities, thus there is no guiding behavior as it happens for π -transitions. Although being presented in arbitrary units, the amplitude scale used for figure 7 is the same as for the π -transitions, allowing to compare the three cases. Each circular polarization gives rise to a group of four r-transitions, all tending to an amplitude (≈ 0.66 a. u.) twice bigger than the amplitude of the π -GTs (≈ 0.33 a. u.). The r-transitions obey the selection rules $\Delta m_I = 0$, $\Delta m_J = \pm 1$ depending on the sign of the incident polarization. A set of absorption spectra is presented in figure 8.

Due to the absence of GTs for circularly polarized incident radiation, less peculiarities occur in this case. One can also note the absence of dipole moment cancellation, as was observed in [34, 41]. However, some observations can still be made from figure 8. Here, the behavior of the r-transitions is somewhat different than before: for σ^+ polarization, the frequency shifts all tend to a linear behavior with a slope twice bigger than for the π -r-transitions. For example, we take a look at transition 11 (σ^-) occurring between the ground state $|2, 2\rangle$ and the excited state $|1, 1\rangle$. Using relation (3), we can easily determine that

$$E_g = \zeta - \mu_B B_z. \quad (17)$$

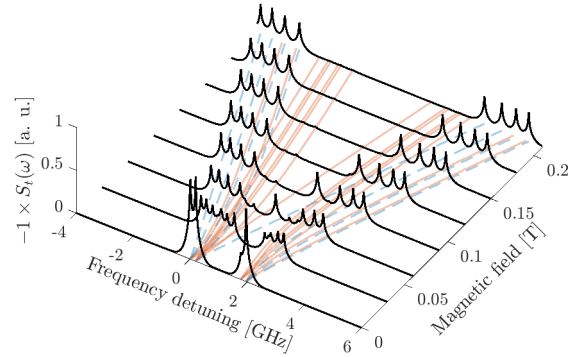


Figure 8: (color online) Absorption spectra of sodium D_1 line for a magnetic field varying from 0 to 0.21 T with a step of 0.03 T in case of simultaneous σ^+ and σ^- excitation. Blue and orange shadow lines in the (x, y) plane represent the transition frequencies. The zero detuning is set to the transition $F_g = 1 \rightarrow F_e = 1$. As before, each peak has a FWHM of approximately 100 MHz.

For the excited state, we only compute the block corresponding to $m_{F_e} = 1$ using relations (3) and (4). This leads to

$$H_e = \begin{pmatrix} X & -\sqrt{3}X \\ -\sqrt{3}X & \zeta' - X \end{pmatrix} \quad (18)$$

where we denoted $X = \mu_B B_z / 6$. Diagonalizing H_e and performing an asymptotic expansion allows to obtain the energy E_e of state $|1, 1\rangle$ for $B_z \gg B_0$:

$$E_e = \frac{\zeta' + [\zeta'^2 - 4\zeta'X + 16X^2]^{1/2}}{2} \underset{X \rightarrow +\infty}{\sim} 2X + \frac{\zeta'}{4} + \frac{3\zeta'^2}{64X} + O\left(\frac{1}{X^2}\right). \quad (19)$$

The difference between (19) and (17) leads to $8X + \zeta'/4 - \zeta + O(1/X)$, thus we obtain the asymptotic slope of the frequency shift of transition 11 (σ^-) and by extension of all σ^\pm -r-transitions:

$$s_{\pm, r}^{D_1^{(\sigma^\pm)}} \approx \mp \frac{4\mu_B}{3}. \quad (20)$$

This method was used before for the D_1 π -transitions and will be used throughout all this paper. As we can see in figure 8, the v-transitions (orange solid lines) that are not overlapped with any r-transition (blue dashed lines) have a frequency shift of slope twice smaller than the value given by relation (20). We present two spectra for $B_z \gg B_0$ in figure 9.

The numerical parameters used for the computation of the spectra are the same as the ones used before in the case of π -transitions. On the top panel, the peaks are overlapped due to the linewidth. However, clear manifestation of the hyperfine Paschen-Back regime is visible on the bottom panel where all the peaks are evenly spaced and have the same amplitude. Due to the fact that the slope of the frequency shifts corresponding to the two groups of r-transitions is twice bigger, the frequency detuning between them can also be roughly estimated by

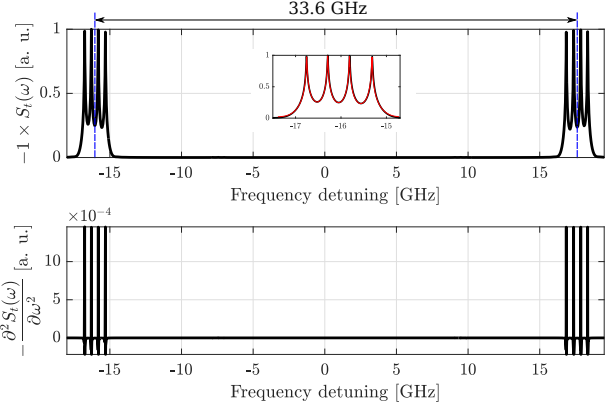


Figure 9: (color online) Absorption spectrum of the D_1 line of sodium for simultaneous σ^\pm polarized incident laser radiation in the hyperfine Paschen-Back regime ($B_z = 0.9$ T). Top: transmitted signal. Bottom: second derivative (SD). Inset: "mirror" overlap of the two groups when the high-frequency group is computed as a function of $-\omega$. The top curve has been normalized so that the maximum amplitude is 1.

$$\Delta\omega_r^{D_1^{(\sigma)}} \approx \left| \frac{8\mu_B B_z}{3} \right|. \quad (21)$$

Here, we obtain $\Delta\omega_r^{D_1^{(\sigma)}} \approx 33.59$ GHz which is in perfect agreement with the value 33.6 GHz measured in figure 9.

In this section, we have provided a complete description of the influence of the magnetic field on the behavior of the Zeeman transitions of sodium D_1 line for the three main types of incident laser radiation. We will now analyze deeply what happens for the D_2 line, with much more transitions, where different phenomena arise.

4. Sodium D_2 line

The D_2 line of sodium corresponds to the transitions occurring between the states $3^2S_{1/2}$ and $3^2P_{3/2}$. Due to the bigger value of J_e , much more transitions are possible than for the D_1 line (in total, 68). Since natural sodium is only composed of one isotope of nuclear spin $I = 3/2$, the hyperfine manifold is simpler than the one of natural rubidium (two isotopes) or cesium (only one isotope but $I = 7/2$). For the numerical computations, we considered the hyperfine splittings $\alpha' = 15.809(80)$ MHz between $F_e = 0$ and $F_e = 1$, $\beta' = 34.344(69)$ MHz between $F_e = 1$ and $F_e = 2$, and $\delta' = 58.326(43)$ MHz between $F_e = 2$ and $F_e = 3$.

4.1. Linearly polarized incident radiation

24 π -transitions are possible for the D_2 line of sodium. A complete scheme as well as the transition intensities are presented in figure 10. In this case, $F_g = 1, 2$ and $F_e = 0, 1, 2, 3$ [4].

The behavior of the π -transitions of sodium D_2 line is quite different from the D_1 line. Firstly, the absence of transitions between uncoupled states results in the absence of guiding transitions. Overall, the general shape is different, and this is due to

the fact that the states experience "more coupling" (for a given spectroscopic state in the case of D_1 line, the magnetic field can couple at most two F -levels, whereas for the D_2 line the coupling goes up to three F levels. Many transition intensities are very small throughout the whole range of magnetic field, and most of them quickly vanish, as seen from the insets of figure 10. Using the same denomination, we denote as r-transitions the transitions 2, 5, 8, 12, 15, 18, 21 and 23 since they obey the selection rules $\Delta m_I = \Delta m_J = 0$, and all the others will be denoted as v-transitions. It is worth noticing that for the D_1 line, we could emphasize the fact that all r-transitions obeyed $\Delta F = 0$. No such rule in the uncoupled basis can be exhibited here. In the previous part, we called as MI the transitions whose intensity was 0 for a very small magnetic field. In figure 10, this phenomenon is clearly visible for r-transitions 5 and 18. For the sake of clarity, labelling is not presented here for the v-transitions although it is completely possible to associate each curve to a given transition. However, this notion of MI transitions can be completed. Here, we will also denote transitions 3, 7, 10 and 16 as Magnetically Induced. All of them are v-transitions, and their amplitude tends to 0 for $B_z \rightarrow 0$, except for transition 3 ($|1, -1\rangle \rightarrow |3', -1\rangle$) which experiences a huge increase in amplitude. Here, MI refers to the fact that, due to the coupling of states by B_z , so-called "forbidden" transitions ($\Delta F = \pm 2$) become possible. Here, we have 3 r-transitions arising from $F_g = 1$ and 5 from $F_g = 2$ (transitions 12 and 23 are exactly overlapped in figure 10). The total number of π -r-transitions is the same as for the D_1 line meaning, and there are much more v-transitions here (16 compared to 6). In figure 11, we present a set of absorption spectra along with the transition frequencies to observe their behavior as the magnetic field increases.

Since the hyperfine splitting of the state ${}^2P_{3/2}$ is much smaller for sodium than for rubidium or cesium [1–4], the peaks are in general much closer here. At zero-field, the 6 peaks remain completely overlapped. Using SD or dSR is a good way to recover the spectral information, as demonstrated on the inset of figure 11 where the relative transition intensities are in perfect agreement with the oscillator strengths presented in [4] ($S_{10} = 1/6$, $S_{11} = S_{12} = 5/12$).

At first, for the same values of magnetic field as before, one notices that all the transitions experiencing the largest frequency shift with respect to the magnetic field are the 16 v-transitions. They can be divided into three groups of same frequency shift (in absolute value). The frequency shifts of the two groups of r-transitions tend asymptotically to a linear behavior with a slope

$$S_{\pm,r}^{D_2^{(\pi)}} \approx \pm \frac{\mu_B}{3} = \frac{S_{\pm,r}^{D_1^{(\pi)}}}{2}. \quad (22)$$

All the slopes are derived using similar procedures used in relations (17) to (20). The v-transitions undergo much bigger frequency shifts, and can be divided into three groups having asymptotically the same slope in absolute value. Under the approximations $g_S \approx 2$, $g_L \approx 1$ and $g_I \ll g_J$, the first group of v-transitions (in terms of proximity with the r-transitions) experi-

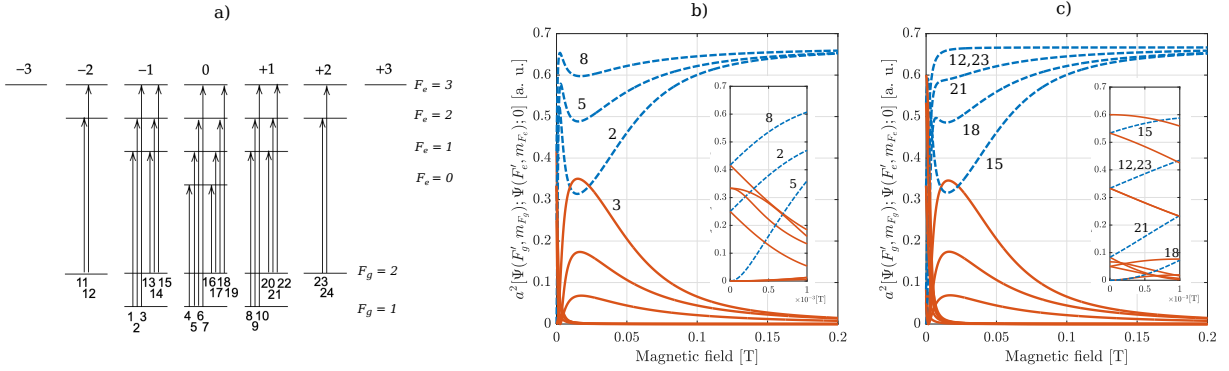


Figure 10: (color online) a) Scheme of all possible π -transitions for the D_2 line of sodium. b) transitions from $F_g = 1$. c) transitions from $F_g = 2$. Respective behavior for very low magnetic field is shown in the insets. The v-transitions are represented in orange (solid lines) and the r-transitions are represented in blue (dashed lines).

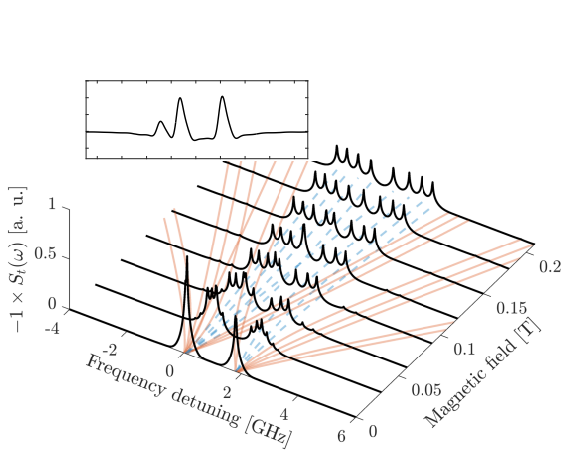


Figure 11: (color online) Absorption spectra of the D_2 line of sodium for π -polarized incident laser radiation. The magnetic field intensity varies from 0 to 0.21 T with a step of 30 mT. The zero frequency is set to the transition $F_g = 1 \rightarrow F_e = 0$. The inset shows the SD of the three peaks $F_g = 1 \rightarrow F_e = 0, 1, 2$.

ences a frequency shift of asymptotic slope $\pm\mu_B$. The frequency shifts of the second group of v-transitions have an asymptotic slope $\pm 5\mu_B/3$. The slope for the last group is $\pm 3\mu_B$. This is consistent with figure 11 where we can see the last group of v-transitions experiencing the biggest shifts (more than 4×10^4 MHz/T, 9 times more than the r-transitions). Numerically, we obtain respectively $\pm 1.40061 \times 10^4$, $\pm 2.29035 \times 10^4$ and $\pm 4.15417 \times 10^4$ MHz/T. A spectrum for $B_z \gg B_0$ is presented in figure 12.

As before, the bottom panel shows that SD is convenient to obtain complete resolution of peaks. Hyperfine Paschen-Back is reached since all the peaks are evenly spaced and tend to the same amplitude. It is again possible to estimate the frequency detuning between the two groups of r-transitions as

$$\Delta\omega_r^{D_2(\pi)} \approx \left| \frac{2\mu_B B_z}{3} \right|. \quad (23)$$

Here, we obtain $\Delta\omega_r^{D_2(\pi)} \approx 8.40$ GHz (by numerical computation, we obtain 8.46 GHz. The small variation is due to the fact

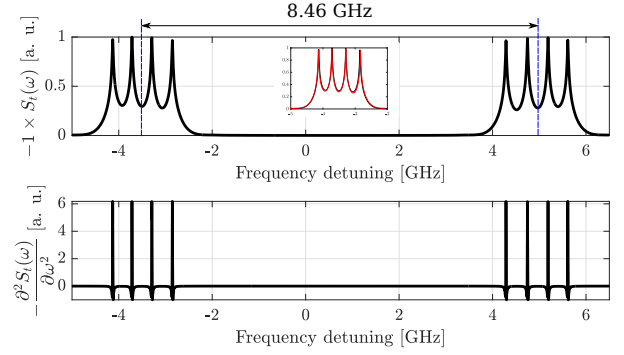


Figure 12: (color online) Top panel: absorption spectrum of the D_2 line of sodium for π -polarized excitation in the hyperfine Paschen-Back regime ($B_z = 0.9$ T). Bottom panel: second derivative (SD). Inset: "mirror" overlap of the two groups when the high-frequency group is computed as a function of $-\omega$. The top curve has been normalized so that the maximum amplitude is 1.

that when calculating the slopes, the hyperfine splittings are neglected.

4.2. Circularly polarized incident laser radiation

44 Zeeman transitions are possible in case of circularly polarized radiation for the D_2 line of sodium. All these possible σ^\pm -transitions are schematized in figure 13.

One directly sees on the manifold presented in figure 13 that, due to the selection rule $\Delta m_F = \pm 1$, transitions between uncoupled states are again possible. These transitions are labelled 10 (σ^-) and 22 (σ^+). They occur between states $|2, \pm 2\rangle$ and $|3, \pm 3\rangle$ depending on the polarization, and obey $\Delta F = 1$. They are again called guiding transitions and their constant amplitude for any magnetic field is clearly visible in figure 14.

For each polarization appears a group of r-transitions (1, 3, 6 and 10 for σ^- and 16, 19, 21, 22 for σ^+) denoted r1-transitions. Transition 10 (σ^-) is a GT for transitions 1, 3 and 6, and transition 22 (σ^+) is a GT for transitions 16, 19 and 21. As we did in relation (14), we can prove that for both of these transitions, the squared modified transfer coefficients a^2 (relation (7)) are always equal to 1. Two other groups of r-transitions, denoted as r2-transitions, represented in purple (dash-dotted lines), ap-

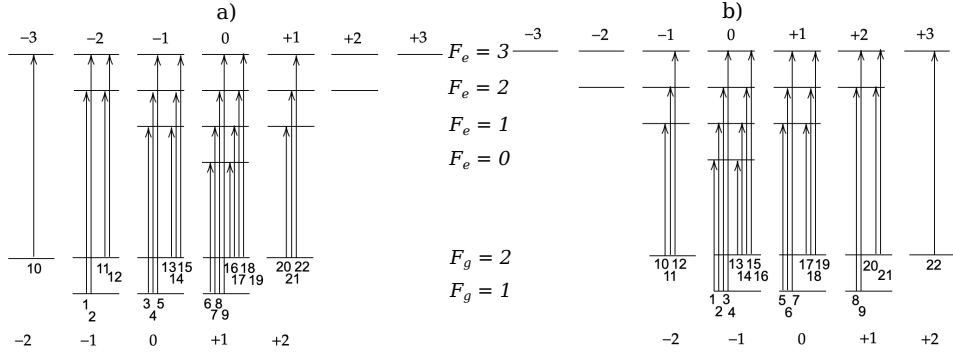


Figure 13: All possible σ^\pm Zeeman transitions for the D_2 line of ^{23}Na in the basis $|F, m_F\rangle$. a) σ^- -transitions. b) σ^+ -transitions.

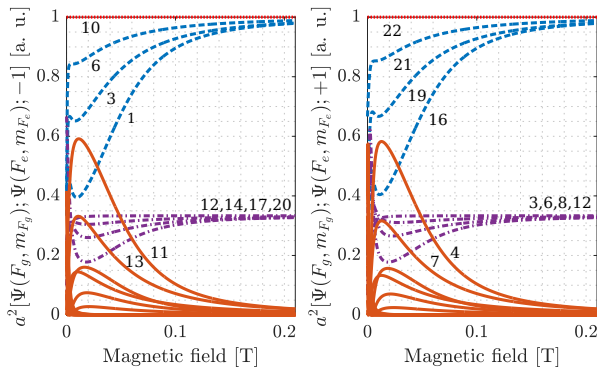


Figure 14: (color online) Sodium hyperfine transition intensities for circularly polarized laser radiation. a) σ^- -transitions. b) σ^+ -transitions. Past $B_0 \approx 0.063$ T, two different groups of transitions have an amplitude that remains considerable. These two different groups are represented in blue (dashed lines) and purple (dash-dotted), and the vanishing transitions are represented in orange. Labelling is consistent with figure 13.

pear and all tend to an amplitude equal to a third the amplitude of the r1-transitions. For both polarization, r2-transitions tend to reach their maximum amplitude much faster than r1-transitions. In orange are represented the vanishing transitions (v-transitions) for each polarizations. Apart from transitions 11 and 13 (σ^-) and transitions 4 and 7 (σ^+), all the v-transitions have overall smaller amplitudes than all r1 and r2-transitions. The 22 possible σ^- -transitions are shown in figure 15. The GT (labelled 10 in figure 13a) has a constant amplitude, and the three other r1-transitions are also driven by the GT in terms of frequency shift. The guiding transition has a perfectly linear frequency shift of slope

$$s_{GT}^{D_2^{(\sigma^-)}} \approx \mu_B, \quad (24)$$

under the usual approximations, the numerical value being $\approx -1.39958 \times 10^4$ MHz/T while $\mu_B = -1.39962 \times 10^4$ MHz/T. The r2-transitions, having an amplitude three times smaller, experience a frequency shift of approximately $5\mu_B/3$ for high enough B_z . Numerically, we obtain approximately -2.331×10^4 MHz/T. As for the previous cases, the v-transitions experience much bigger frequency shifts, reaching again as much as approxi-

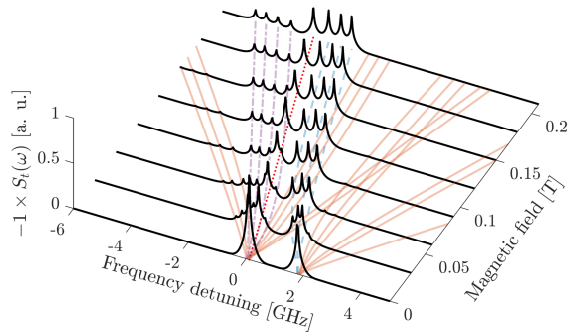


Figure 15: (color online) Absorption spectra of the D_2 line of sodium for σ^- -polarized incident laser radiation. The magnetic field intensity varies from 0 to 0.21 T with a step of 30 mT. The zero frequency is set to the transition $F_g = 1 \rightarrow F_e = 0$.

mately $3\mu_B = -4.199 \times 10^4$ MHz/T (numerically, -4.202×10^4 MHz/T). The behavior of the σ^+ is reversed compared to σ^- , as we can see in figure 16.

The guiding transition (in this case 22) experiences a frequency shift $s_{GT}^{D_2^{(\sigma^+)}} = -s_{GT}^{D_2^{(\sigma^-)}}$ and so do all the r1-transitions when B_z is high enough so that the frequency shift becomes linear. The r2-transitions will also similarly experience a linear frequency shift $-5\mu_B/3$ (numerically, $\approx 2.331 \times 10^4$ MHz/T). When the hyperfine Paschen-Back regime is reached ($B_z > 10B_0$), only the r1 and r2-transitions of each polarization remain visible in the spectrum (16 peaks in total). This is clearly demonstrated in figure 17 where the spectrum is presented in case of simultaneous σ^\pm excitation for $B_z = 0.9$ T.

From the obtained slopes, we can estimate that the frequency detuning between the two groups of r1-transitions is approximately

$$\Delta\omega_{r1}^{D_2^{(\sigma)}} \approx |2\mu_B B_z|, \quad (25)$$

leading to $\Delta\omega_{r1}^{D_2^{(\sigma)}} \approx 25.19$ GHz, perfectly consistent with the value 25.15 GHz on the top panel of figure 17, with the dif-

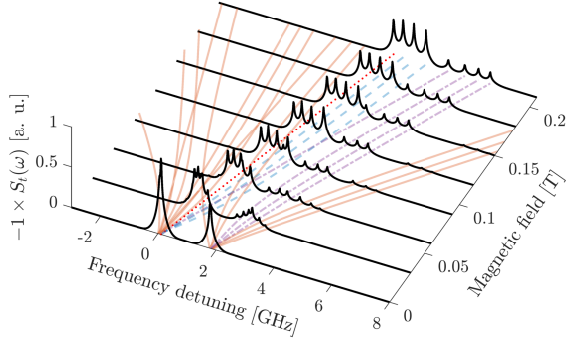


Figure 16: (color online) Absorption spectra of the D_2 line of sodium for σ^+ -polarized incident laser radiation. The zero frequency is set to the transition $F_g = 1 \rightarrow F_e = 0$.

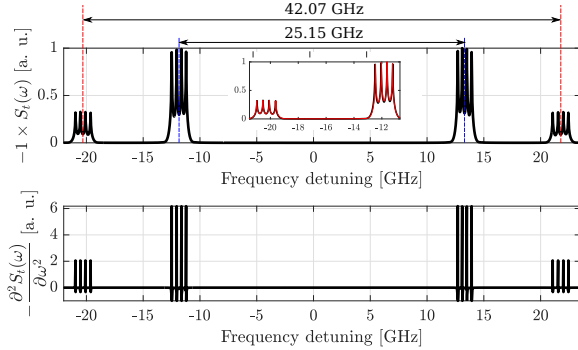


Figure 17: (color online) Top panel: absorption spectrum of the D_2 line of sodium for simultaneous σ^\pm polarized excitation in the hyperfine Paschen-Back regime ($B_z = 0.9$ T). Bottom panel: second derivative (SD).

ference coming from the fact that hyperfine splittings are neglected. Similarly, we can estimate $\Delta\omega_{r2}^{D_2^{(\sigma)}}$ to be

$$\Delta\omega_{r2}^{D_2^{(\sigma)}} \approx \left| \frac{10\mu_B B_z}{3} \right| \quad (26)$$

that is to say approximately 41.98 GHz, to compare with the value 42.07 GHz of figure 17.

Reaching hyperfine Paschen-Back regime combined with sub-Doppler spectroscopic techniques allows to form narrow resonances far-detuned from the resonant frequency of the transitions. Choosing the right alkali atom for such studies is a key point since B_0 varies a lot. Hyperfine splittings and natural linewidths are also to take into account depending on the desired resolution. We will now focus on the so-called forbidden transitions, obeying $\Delta F = \pm 2$. Their intensities are plotted in figure 18.

At first glance, what can be observed in figure 18 is the overall difference in intensity between the two polarizations: while v-transition 2 (σ^- , hereafter denoted 2^-) peaks at approximately 0.16, v-transition 4 $^+$ peaks at nearly 0.6 (both panels have the same Y-scale). These transitions arise from the same ground

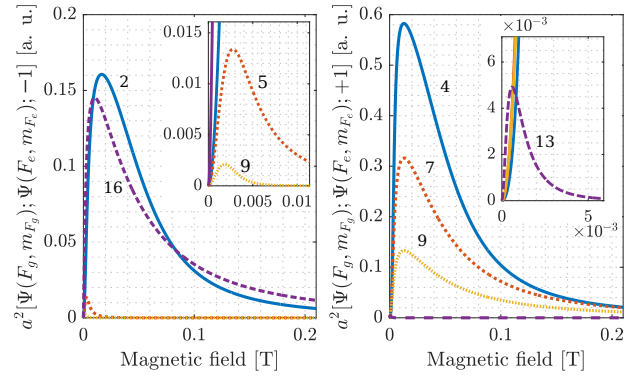


Figure 18: (color online) Intensities of transitions obeying $\Delta F = \pm 2$. a) σ^- -transitions. b) σ^+ -transitions. The insets show the very-low-field behavior of transitions having a very small intensity. Labelling is consistent with figure 13.

state $|1, -1\rangle$, and 2^- (resp. 4^+) goes to $|3, -2\rangle$ (resp. $|3, 0\rangle$) due to the selection rule on Δm_F and obey $\Delta F = +2$. The inverse behavior can be observed for v-transitions 16^- and 13^+ : their ground states are different, respectively $|2, -1\rangle$ and $|2, +1\rangle$, but they have the same excited state $|0, 0\rangle$. They obey $\Delta F = -2$. Transition 16^- reaches a little more than 0.14, while transition 13^+ only reaches 5×10^{-3} . To observe this behavior more clearly, the ratios $I(4^+)/I(2^-)$ and $I(16^-)/I(13^+)$ are presented in figure 19. We call group G2 $^+$ the transitions obeying $\Delta F = +2$, and group G2 $^-$ the transitions obeying $\Delta F = -2$.

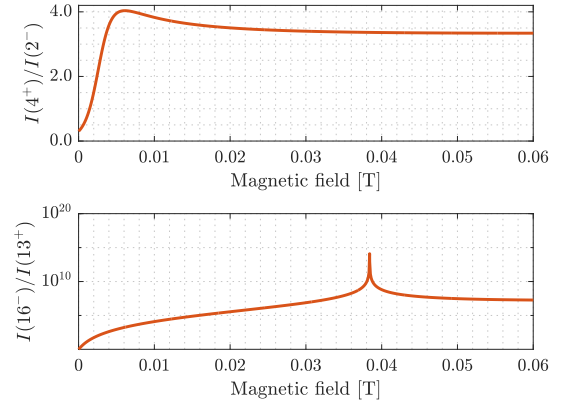


Figure 19: (color online) Intensity ratio between the two strongest MI-transitions of their group. Top panel: MI-transitions obeying $\Delta F = +2$ (group G2 $^+$, $I(4^+)/I(2^-)$). Bottom panel: MI-transitions obeying $\Delta F = -2$ (group G2 $^-$, $I(16^-)/I(13^+)$).

The ratio $I(4^+)/I(2^-)$ has a maximum of approximately 4, occurring for $B_z \approx 6.12$ mT, whereas on the bottom panel $I(16^-)/I(13^+)$ reaches as much as 1.25×10^{14} for $B_z \approx 38.41$ mT. This phenomenon is referred to as Magnetically-induced Circular Dichroism (MCD) or frequency-controllable circular dichroism: for $\Delta F = +2$, the strongest σ^+ transition intensity is more than 4 times higher than the strongest σ^- one, and for $\Delta F = -2$, σ^- transitions are stronger than σ^+ . By varying the laser frequency and its polarization, it is thus possible to choose

whether σ^+ or σ^- MI-transition will dominate. The figure of merit coefficient allows, for each group, to better visualize the dichroism phenomenon. It is defined as

$$C_{MCD} = \frac{I^+ - I^-}{I^+ + I^-} \quad (27)$$

and is represented for the aforementioned transitions in figure 20.

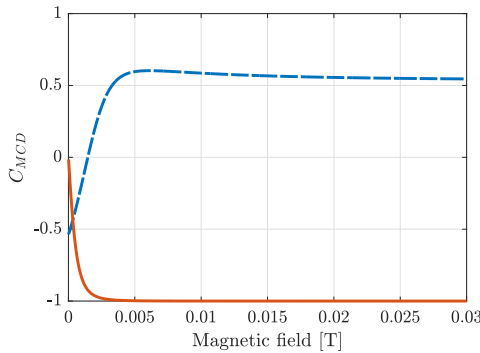


Figure 20: (color online) Figure of merit coefficient C_{MCD} for each group of transitions. Blue (dashed line): $(I(4^+) - I(2^-))/(I(4^+) + I(2^-))$. Orange (solid line): $(I(13^+) - I(16^-))/(I(13^+) + I(16^-))$.

The coefficient defined in relation (27) can be interpreted as follows: $C_{MCD} = 0$ represents equality between the intensities of the two strongest MI-transitions (one per polarization) of each group. $C_{MCD} > 0$ (resp. $C_{MCD} < 0$) means that the strongest transition occurs for σ^+ (resp. σ^-) thus leading to an asymmetry. $C_{MCD} = -1$, which is the case for the orange curve of figure 20 (transitions belonging to group G2 $^-$), means complete vanishing of the σ^+ transition and is reached for $B_z > 3$ mT. This type of MCD is referred to as Type 1 MCD, and has been thoroughly described and observed for other alkali (Rb and Cs in [30] and [20]).

Moreover, it was recently demonstrated in [19] (theoretically and experimentally, by using a Cs-filled nanocell) that even among the strongest MI-transitions arising from different ground states for each circular polarization, the strongest MI-transition obeying $\Delta F = +2$ is always bigger than the strongest MI-transitions obeying $\Delta F = -2$. This is verified here: transition 4 $^+$ ($|1, -1\rangle \rightarrow |3, 0\rangle$) is stronger than 16 $^-$ ($|2, 1\rangle \rightarrow |0, 0\rangle$). Numerically, here it is verified for the range 2.4 mT - 1 T. As mentioned in [19], calculations suggest that Type 1 and Type 2 MCD could be observed for other first fundamental series of $nS \rightarrow nP D_2$ lines, where MI-transitions also occur.

5. Conclusion

In this paper, we have performed a complete theoretical description of the behavior of a ^{23}Na vapor confined in a nanometric-thin cell for a wide range of magnetic field (varying up to 1 Tesla) and for three incident laser polarizations (linear, left and right-circular). While the Zeeman structure of sodium is identical to the one of ^{87}Rb or ^{39}K , several changes can be reported such as B_0 and the hyperfine splittings, leading to slight

changes in the behavior of transition intensities and transition frequencies. As mentioned before, the natural linewidth Γ_{nat} of sodium is twice bigger than for other alkalis, and leads to much broader absorption lines. However, for the same temperature the vapor pressure of sodium is much smaller than for heavier alkali atoms ($\approx 10^{-7}$ torr, whereas for cesium it is $\approx 6 \times 10^{-4}$ torr and $\approx 2.5 \times 10^{-4}$ torr for ^{85}Rb). This leads to smaller collisional broadening, but also makes the transmitted and reflected signal smaller so that either a higher temperature or more sensitive detectors would be required to record the signal when performing experiments. In addition, we provided in this paper rough estimates of the frequency detuning between the various groups of transitions that remain present in the spectra when the hyperfine Paschen-Back regime is reached. We highlighted for the first time the appearance of Type 1 and Type 2 circular dichroism in a sodium vapor, and provided high-resolution absorption spectra of sodium Zeeman transitions depending on the external magnetic field.

Complete description and understanding of all these magneto-optical processes are of utmost importance for further applications, for example in optical magnetometry. Upcoming experiments involving nanocells are planned at the Institute for Physical Research, NAS of Armenia, to provide an experimental verification of these results. Complete agreement between experiments and theory is expected as it was proven for all other alkalis (except lithium, for which it is very hard to fabricate a nanocell).

Acknowledgments - Funding information

R. Momier acknowledges the support of the program "Investissements d'Avenir" - project ISITE-BFC (contract ANR-15-IDEX-0003) and wishes to thank UBFC International Relations office for handling administrative tasks, as well as the Institute for Physical Research, NAS of Armenia, for their welcome. This research was sponsored in part by the NATO Science for Peace and Security Programme under grant G5794.

Declaration of competing interests

The authors declare that they have no known competing financial interests or personal relationships that could have appeared to influence the work reported in this paper.

References

- [1] D. Steck, Rubidium 85 D Line Data (2019). URL <https://steck.us/alkalidata/rubidium85numbers.pdf>
- [2] D. Steck, Rubidium 87 D Line Data (2003). URL <https://steck.us/alkalidata/rubidium87numbers.1.6.pdf>
- [3] D. Steck, Cesium D Line Data (2003). URL <https://steck.us/alkalidata/cesiumnumbers.1.6.pdf>
- [4] D. Steck, Sodium D Line Data (2003). URL <https://steck.us/alkalidata/sodiumnumbers.1.6.pdf>
- [5] E. Arimondo, M. Inguscio, P. Violino, Experimental determinations of the hyperfine structure in the alkali atoms, Rev. Mod. Phys. 49 (1977) 31–75. doi:10.1103/RevModPhys.49.31.

- [6] T. G. Tiecke, Properties of Potassium (2019).
URL <https://tobiastiecke.nl/archive/PotassiumProperties.pdf>
- [7] M. E. Gehm, Properties of ^6Li (2003).
URL <https://physics.ncsu.edu/jet/techdocs/pdf/PropertiesOfLi.pdf>
- [8] D. Budker, W. Gawlik, D. F. Kimball, S. M. Rochester, V. V. Yashchuk, A. Weis, Resonant nonlinear magneto-optical effects in atoms, *Rev. Mod. Phys.* 74 (2002) 1153–1201. doi:10.1103/RevModPhys.74.1153.
- [9] S. Bhushan, V. S. Chauhan, M. Dixith, R. K. Easwaran, Effect of magnetic field on a multi window ladder type electromagnetically induced transparency with ^{87}Rb atoms in vapour cell, *Phys. Lett. A* 383 (125885) (2019). doi:10.1016/j.physleta.2019.125885.
- [10] M. Bhattarai, V. Bharti, V. Natarajan, A. Sargsyan, D. Sarkisyan, Study of EIT resonances in an anti-relaxation coated Rb vapor cell, *Phys. Lett. A* 383 (2019) 91–96. doi:10.1016/j.physleta.2018.09.036.
- [11] Z. Tao, M. Chen, Z. Zhou, B. Ye, J. Zeng, H. Zheng, Isotope ^{87}Rb Faraday filter with a single transmission peak resonant with atomic transition at 780 nm, *Opt. Express* 27 (2019) 13142–13149. doi:10.1364/OE.27.013142.
- [12] J. Keaveney, S. A. Wrathmall, C. S. Adams, I. G. Hughes, Optimized ultra-narrow atomic bandpass filters via magneto-optic rotation in an unconstrained geometry, *Opt. Lett.* 43 (2018) 4272–4275. doi:10.1364/OL.43.004272.
- [13] E. Klinger, H. Azizbekyan, A. Sargsyan, C. Leroy, D. Sarkisyan, A. Papoyan, Proof of the feasibility of a nanocell-based wide-range optical magnetometer, *Appl. Opt.* 59 (2020) 2231–2237.
- [14] R. S. Mathew, F. Ponciano-Ojeda, J. Keaveney, D. J. Whiting, I. G. Hughes, Simultaneous two-photon resonant optical laser locking (STROLLing) in the hyperfine Paschen–Back regime, *Opt. Lett.* 43 (2018) 4204–4207. doi:10.1364/OL.43.004204.
- [15] D. Sarkisyan, D. Bloch, A. Papoyan, M. Ducloy, Sub-Doppler spectroscopy by sub-micron thin Cs vapour layer, *Opt. Comm.* 200 (2001) 201–208. doi:10.1016/S0030-4018(01)01604-2.
- [16] A. Sargsyan, A. Papoyan, H. I. G., C. S. Adams, D. Sarkisyan, Selective reflection from an Rb layer with a thickness below $\lambda/12$ and applications, *Opt. Lett.* 42 (2017) 1476–1479. doi:10.1364/OL.42.001476.
- [17] A. Sargsyan, G. Hakhumyan, A. Papoyan, D. Sarkisyan, A. Atvars, M. Auzinsh, A novel approach to quantitative spectroscopy of atoms in a magnetic field and applications based on an atomic vapor cell with $L = \lambda$, *Appl. Phys. Lett.* 93 (021119) (2008). doi:10.1063/1.2960346.
- [18] P. Tremblay, A. Michaud, M. Levesque, S. Thériault, M. Breton, J. Beaubien, N. Cyr, Absorption profiles of alkali-metal D lines in the presence of a static magnetic field, *Phys. Rev. A* 42 (1990) 2766–2773. doi:10.1103/PhysRevA.42.2766.
- [19] A. Sargsyan, A. Amiryan, A. Tonoyan, E. Klinger, D. Sarkisyan, Circular dichroism in atomic vapors: Magnetically induced transitions responsible for two distinct behaviors, *Phys. Lett. A* 390 (127114) (2021). doi:10.1016/j.physleta.2020.127114.
- [20] A. Tonoyan, A. Sargsyan, E. Klinger, G. Hakhumyan, C. Leroy, M. Auzinsh, A. Papoyan, D. Sarkisyan, Circular dichroism of magnetically induced transitions for D2 lines of alkali atoms, *EPL* 121 (53001) (2018). doi:10.1209/0295-5075/121/53001.
- [21] E. Klinger, A. Sargsyan, A. Tonoyan, G. Hakhumyan, A. Papoyan, C. Leroy, D. Sarkisyan, Magnetic field-induced modification of selection rules for Rb D_2 line monitored by selective reflection from a vapor nanocell, *Eur. Phys. J. D* 71 (216) (2017). doi:10.1140/epjd/e2017-80291-6.
- [22] A. Amiryan, Formation of narrow optical resonances in thin atomic vapor layers of Cs, Rb, K and applications, Ph.D Thesis, Université Bourgogne Franche-Comté ; Institute for Physical Research (2019).
URL <https://tel.archives-ouvertes.fr/tel-02318372>
- [23] A. Sargsyan, A. Amiryan, E. Klinger, D. Sarkisyan, Features of magnetically-induced atomic transitions of the Rb D_1 line studied by a Doppler-free method based on the second derivative of the absorption spectra, *J. Phys. B: At. Mol. Opt. Phys.* 53 (185002) (2020).
- [24] A. Sargsyan, A. Amiryan, D. Sarkisyan, Coherent Dicke Narrowing of Absorption Spectra, Collapse and Revival: Second-Derivative Processing, *J. Exp. Theor. Phys.* 131 (2020) 220–226. doi:10.1134/S1063776120050179.
- [25] C. Umfer, L. Windholz, M. Musso, Investigation of the sodium and lithium D-lines in strong magnetic fields, *Z. Phys. D: At. Mol. Clusters* 25 (1992) 23–29. doi:10.1007/BF01437516.
- [26] H. Hidenobu, M. Masaharu, D. Muneyuki, Paschen-Back Effect of D-Lines in Sodium under a High Magnetic Field, *J. Phys. Soc. Jpn.* 51 (5) (1982) 1566–1570. doi:10.1143/JPSJ.51.1566.
- [27] R. González-Férez, P. Schmelcher, Sodium in a strong magnetic field, *Eur. Phys. J. D* 23 (2003) 189–199. doi:10.1140/epjd/e2003-00031-y.
- [28] T. Fan, L. Zhang, X. Yang, S. Cui, T. Zhou, Y. Feng, Magnetometry using fluorescence of sodium vapor, *Opt. Lett.* 43 (2018) 1–4. doi:10.1364/OL.43.000001.
- [29] M. Auzinsh, D. Budker, S. M. Rochester, *Optically Polarized Atoms : Understanding Light-Atom Interactions*, Oxford University Press, 2010.
- [30] E. Klinger, Selective reflection spectroscopy of alkali vapors confined in nanocells and emerging sensing applications, Ph.D Thesis, Université Bourgogne Franche-Comté ; Institute for Physical Research (2019).
URL <https://tel.archives-ouvertes.fr/tel-02317761>
- [31] E. Alexandrov, M. Chaika, G. Khvostenko, *Interference of Atomic States*, Springer-Verlag, 1993.
- [32] G. Breit, I. I. Rabi, Measurement of Nuclear Spin, *Phys. Rev.* 38 (1931) 2082–2083. doi:10.1103/PhysRev.38.2082.2.
- [33] E. Tiesinga, P. Mohr, D. Newell, B. Taylor, The 2018 CODATA recommended values of the fundamental physical constants (2020).
URL <http://physics.nist.gov/constants>
- [34] R. Momier, A. Aleksanyan, E. Gazazyan, A. Papoyan, C. Leroy, New standard magnetic field values determined by cancellations of ^{85}Rb and ^{87}Rb atomic vapors $5^2S_{1/2} \rightarrow 6^2P_{1/2,3/2}$ transitions, *J. Quant. Spectrosc. Radiat. Transf.* 257 (107371) (2020). doi:10.1016/j.jqsrt.2020.107371.
- [35] A. Sargsyan, A. Tonoyan, G. Hakhumyan, A. Papoyan, E. Mariotti, D. Sarkisyan, Giant modification of atomic transition probabilities induced by a magnetic field: forbidden transitions become predominant, *Laser Phys. Lett.* 11 (055701) (2014). doi:10.1088/1612-2011/11/5/055701.
- [36] A. Sargsyan, E. Klinger, A. Tonoyan, C. Leroy, D. Sarkisyan, Hyperfine Paschen–Back regime of potassium D_2 line observed by Doppler-free spectroscopy, *J. Phys. B: At. Mol. Opt. Phys.* 51 (145001) (2018). doi:10.1088/1361-6455/aac735.
- [37] A. Sargsyan, G. Hakhumyan, C. Leroy, Y. Pashayan-Leroy, A. Papoyan, D. Sarkisyan, Hyperfine Paschen–Back regime realized in Rb nanocell, *Opt. Lett.* 37 (2012) 1379–1381. doi:10.1364/OL.37.001379.
- [38] G. Dutier, S. Saltiel, D. Bloch, M. Ducloy, Revisiting optical spectroscopy in a thin vapor cell: mixing of reflection and transmission as a Fabry–Perot microcavity effect, *J. Opt. Soc. Am. B* 20 (2003) 793–800. doi:10.1364/JOSAB.20.000793.
- [39] R. H. Romer, R. H. Dicke, New Technique for High-Resolution Microwave Spectroscopy, *Phys. Rev.* 99 (1955) 532–536. doi:10.1103/PhysRev.99.532.
- [40] T. Vartanyan, D. Lin, Enhanced selective reflection from a thin layer of a dilute gaseous medium, *Phys. Rev. A* 51 (1995) 1959–1964. doi:10.1103/PhysRevA.51.1959.
URL <https://link.aps.org/doi/10.1103/PhysRevA.51.1959>
- [41] A. Aleksanyan, R. Momier, E. Gazazyan, A. Papoyan, C. Leroy, Transition cancellations of ^{87}Rb and ^{85}Rb atoms in a magnetic field, *J. Opt. Soc. Am. B* 37 (2020) 3504–3514. doi:10.1364/JOSAB.403862.
- [42] A. Aleksanyan, R. Momier, E. Gazazyan, A. Papoyan, C. Leroy, All alkali atoms D_1 line magnetic field values cancelling transitions (2020). arXiv:2008.03581.
- [43] A. Sargsyan, A. Tonoyan, G. Hakhumyan, C. Leroy, Y. Pashayan-Leroy, D. Sarkisyan, Atomic transitions of Rb, D_2 line in strong magnetic fields: Hyperfine Paschen–Back regime, *Opt. Comm.* 334 (2015) 208–213. doi:10.1016/j.optcom.2014.08.022.
- [44] W. Demtröder, *Atoms, Molecules and Photons*, Springer-Verlag, 2010.

Conclusion and outlook

In this report, we have provided the theoretical model used to describe the interaction of cw laser radiation with an alkali vapor of nanometric thickness, with and without applying an external magnetic field. In the limit of weak incident laser radiation (linear regime approximation), the FP-cavity model described in Chapter 2 is a convenient way to compute absorption and SR spectra. In this regime, one can obtain the spectra without solving the Liouville equation of the system, which can quickly become a time-consuming process.

Throughout this internship, three main topics were studied:

Using a homemade sensitive photodetector, we managed to record absorption and fluorescence spectra of the D lines of a cesium vapor at nearly room temperature, where the atomic density is very small. Several things can be noted:

- The absorption linewidth narrows down to up to 6 times smaller than the Doppler broadening, allowing to study the power broadening induced by the incident laser.
- The study was performed without applying a magnetic field. Indeed, the hyperfine peaks split into Zeeman peaks but with a much weaker amplitude, as seen in Chapter 3. Since the atomic density is small, the Zeeman peaks' amplitudes were of the order of the noise and not observable, even by applying second derivative techniques.
- Perfect agreement between the theory developed in Chapter 2 and the experimental results was obtained, since the linewidth is a fittable parameter. The transmission lineshape was pseudo-Voigt as expected and the relative transition strengths were consistent with the ones of table A.1. One expects slightly broader spectra for fluorescence, notably due to reabsorption of radiation by the vapor. The theoretical calculations for fluorescence require solving the Liouville equations since the fluorescence signal is proportional to the coherences [31] and still need to be performed.

The second part of this internship was dedicated to the study of the behavior of a nanometric-thin sodium vapor inside a magnetic field varying up to 1 T applied along the laser propagation direction. These results are still purely theoretical due to the lack of laser sources of spectroscopic quality operating in the wavelength range of sodium. Such sources are expected to be available shortly, thus allowing to check the results experimentally. The quantum system is, however, equivalent to ^{87}Rb and ^{39}K , thus we expect total agreement. Some parameters will still need to be taken into account:

- Sodium D lines have natural linewidths nearly twice bigger than the other alkalis, thus one expects at first to see much broader absorption lines.
- The vapor pressure of sodium is much smaller than for the other alkali atoms. This will lead to a much smaller absorption amplitude. Either sensitive detectors will be needed to observe properly the signal, or the vapor will need to be heated more than for other alkalis. Due to the smaller vapor pressure, one also expects smaller collisional broadening. However, this broadening is typically very small.

In the accepted preprint

- R. Momier, A. Papoyan and C. Leroy, "Sub-Doppler spectra of sodium D lines in a wide range of magnetic field: theoretical study", accepted by *J. Quant. Spectrosc. Radiat. Transf.* (June 1st, 2021), arXiv:2104.14896.

we describe for the first time precise sub-Doppler spectral features of the D lines of sodium as well as the magneto-optical peculiarities that occur throughout the whole range of magnetic field. Such processes are widely studied for other alkalis and find notable applications in optical magnetometry [13]. Moreover, the smaller B_0 value of sodium (four times smaller than B_0 of ^{87}Rb , nearly three times smaller than B_0 of ^{133}Cs) makes it a promising candidate for applications relying on the hyperfine Paschen-Back regime, such as laser frequency stabilization, due to the possibility of creating far-detuned (several GHz) narrow resonances with a much smaller magnetic field than usual (along with natural potassium).

The last part of this internship was dedicated to the study of possible signature of Rabi oscillations in the transmission signal of a nanocell. In [43], FFT analysis of the transmitted signal (on a very short timescale, a few tens of nanoseconds) of a 7 cm-long natural rubidium cell revealed power- and detuning-dependent peaks which were associated to manifestations of generalized Rabi frequencies. One of the goals was to reproduce these results with a cesium nanocell. Unfortunately, such behavior could not be observed in the nanocell at a thickness $L \approx \lambda$, since the FFT amplitude ended up being nearly 1000 times smaller than the FFT amplitude obtained with the regular long cell. It is yet unclear whether this variation only arises due to the smaller atomic density, or whether it is linked to thickness-related effects such as atom-surface interactions. Seemingly satisfactory results were obtained with a room temperature 1 cm-long cesium cell, suggesting that the cell thickness is a key parameter in this effect. FFT peaks were observed in the transmission signal of a 40 μm -long cell, however, these peaks were not power- and detuning-dependent. After further analysis, they were associated to a manifestation of the internal frequency stabilization system of the laser. It is worth nothing that the experiments were performed with much narrower laser than the one used in [43], and it is also yet unclear whether the laser linewidth has a notable influence on the results.

Appendix A

Additional information

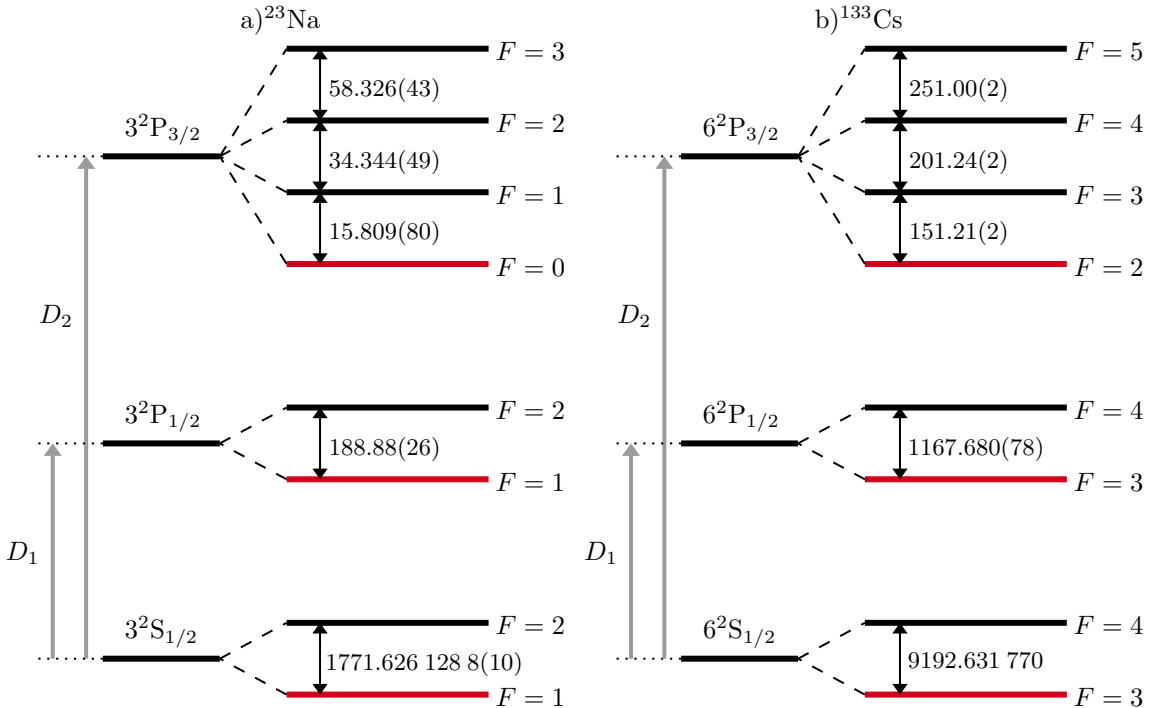


Figure A.1: a) Fine and hyperfine structure of ^{23}Na D lines. b) Fine and hyperfine structure of ^{133}Cs D lines. The hyperfine splittings are given in MHz with their uncertainty. The states represented with red lines are set as energy references in the computations and the grey arrows represent the D_1 and D_2 optical transitions, see table A.1 for the transition wavelengths (nm) and frequencies (THz). Diagrams adapted from [3, 4].

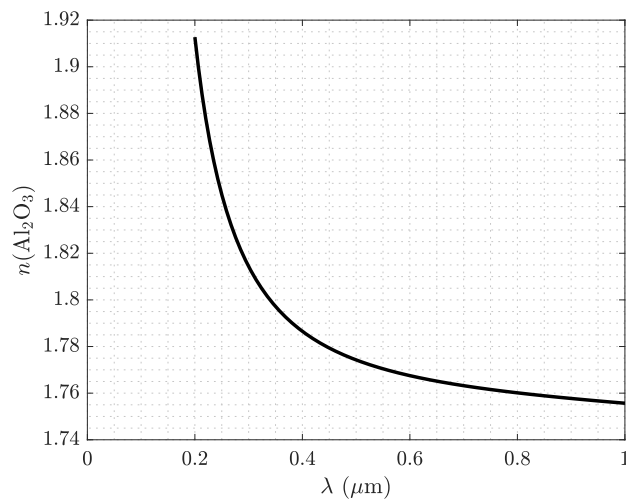


Figure A.2: Refractive index of sapphire as a function of the wavelength (μm).

	Notation	^{23}Na	Ref.	^{133}Cs	Ref.	
Atomic number	Z	11		55		
Abundance (%)	η	100	[44]	100	[44]	
Principal quantum number	n	3		6		
Atomic mass (u)	m_a	22.989 769 280 7(28)	[45]	132.905 451 931(27)	[45]	
Nuclear spin	I	3/2		7/2		
Magnetic dipole constant ($\text{h}\cdot\text{MHz}$)	$A_{n^2S_{1/2}}$	885.813 064 4(5)	[6]	2298.157 9425	[6]	
	$A_{n^2P_{1/2}}$	94.44(13)	[46]	291.920(19)	[47, 48]	
	$A_{n^2P_{3/2}}$	18.534(15)	[49]	50.275(3)	[50]	
Electric quadrupole constant ($\text{h}\cdot\text{MHz}$)	$B_{n^2P_{3/2}}$	2.724(30)		-0.53(2)		
	g_S	2.002 319 304 362 56(35)	[35]	2.002 319 304 362 56(35)	[35]	
	g_L	0.999 976 13	[4]	0.999 995 87	[3]	
Landé factors	g_I	-0.000 804 610 8(8)	[6]	0.000 398 853 95(52)	[6]	
	$g_J(n^2S_{1/2})$	g_S		g_S		
	$g_J(n^2P_{1/2})$	0.665 861 738 545...	Recalculated	0.665 888 058 545...	Recalculated	
	$g_J(n^2P_{3/2})$	1.334 090 521 454...		1.334 103 681 454...		
	λ_{D_1}	589.598 53	[4]	894.353 09	[3]	
Transition wavelength in air (nm)	λ_{D_2}	589.000 35		852.118 73		
	$\omega_0^{D_1}$	508.3324657		335.116048807		
Transition frequency ($2\pi\cdot\text{THz}$)	$\omega_0^{D_2}$	508.8487162		351.72571850		
	γ_{D_1}	9.765(13)		4.561 2(57)		
Natural linewidth (FWHM, $2\pi\cdot\text{MHz}$)	γ_{D_2}	9.795(11)		5.222 7(66)		
	$S_{FF'}(D_1)$	$S_{11} = 1/6$	Recalculated	$S_{33} = 1/4$	Recalculated	
Relative transition strength $F \rightarrow F'$		$S_{12} = 5/6$		$S_{34} = 3/4$		
		$S_{10} = 1/6$		$S_{32} = 5/14$		
		$S_{11} = 5/12$		$S_{33} = 3/8$		
		$S_{12} = 5/12$		$S_{34} = 15/56$		
		$S_{21} = 1/2$		$S_{43} = 7/12$		
$S_{FF'}(D_2)$	$S_{22} = 1/2$	$S_{44} = 5/12$				
	$S_{21} = 1/20$	$S_{43} = 7/72$				
	$S_{22} = 1/4$	$S_{44} = 7/24$				
	$S_{23} = 7/10$	$S_{45} = 11/18$				

Table A.1: Summary of different physical and optical constants of ^{23}Na and ^{133}Cs , with their respective unit. When possible, the uncertainty on the value and the bibliographic reference are provided.

Appendix B

Linear interaction regime

Doppler-broadened two-level systems have been extensively treated in [33, 51, 52]. Here, we assume that

- Atoms leave the cell wall in the ground state
- The incident laser beam diameter greatly exceeds the cell thickness
- The medium is optically thin (that is $E_t'' \ll E_t'$, see equations (2.14) and (2.15)) and dilute enough so that only atom-surface collisions are considered.

If the atomic response is linear with respect to the incident field, one can express the forward and backward integrals (2.13) of the atomic response as

$$I_f = I_T^{lin} - r_2 I_{SR}^{lin} \quad (\text{B.1})$$

$$I_b = I_{SR}^{lin} - r_2 \exp(2ikL) I_T^{lin}, \quad (\text{B.2})$$

where I_T^{lin} and I_{SR}^{lin} are given by

$$I_T^{lin} = C \int_{-\infty}^{+\infty} W(v) g(\Delta, v, L) dv \quad (\text{B.3})$$

$$I_{SR}^{lin} = C \int_{-\infty}^{+\infty} W(v) h_{\pm}(\Delta, v, L) dv = C \int_{-\infty}^0 W(v) h_{-}(\Delta, v, L) dv + C \int_0^{+\infty} W(v) h_{+}(\Delta, v, L) dv. \quad (\text{B.4})$$

Equations (B.3) and (B.4) are the transmitted and reflected lineshapes in the linear interaction regime arising from spatial integration of the transient atomic response. They depend on the speed v of the atoms inside the vapor obeying the Maxwell-Boltzmann distribution defined in Chapter 1. Obviously, the lineshape depends on the laser detuning $\Delta = \omega - \omega_0$, where ω_0 is the resonant angular frequency of the two-level medium. The function g and h are given by

$$g(\Delta, v, L) = -\frac{k}{\Lambda_+} \left\{ L - \frac{|v|}{\Lambda_+} \left[1 - \exp \left(-\frac{\Lambda_+ L}{|v|} \right) \right] \right\} \quad (\text{B.5})$$

$$h(\Delta, v, L) = \frac{1}{2i} \left[\frac{1}{\Lambda_{\mp}} - \frac{\exp(2ikL)}{\Lambda_{\pm}} \right] - \frac{k|v|}{\Lambda_+ \Lambda_-} \exp \left(-\frac{\Lambda_{\mp} L}{|v|} \right) \quad (\text{B.6})$$

$$\Lambda_{\pm} = \gamma - i\Delta \pm ikv \quad (\text{B.7})$$

where γ is the natural linewidth of the two-level medium (figure 2.2). The linewidth γ in this model is a free parameter that can be modified to take into account additional homogeneous (e.g. collisional) or inhomogeneous (e.g residual Doppler) broadenings. The constant C is given by

$$C = \frac{N_D \mu_{eg}^2 t_{10} E_i}{4\hbar F \epsilon_0}, \quad (\text{B.8})$$

where N_D is the number density defined in Chapter 1, \hbar is the reduced Planck constant, ϵ_0 is the vacuum permittivity and μ_{eg} is the transition dipole momentum. Finally, one can build a numerical simulation allowing to obtain the reflection and transmission lineshape of a given two-level system:

- Initialization of the resonant frequency and detuning array $\Delta = \omega - \omega_0$.
- Computation of $W(v)$ and equation (B.7) for all velocities.
- Injection of (B.7) into (B.5) and (B.6).
- Numerical integration of (B.3) and (B.4) with bounds $v_B = \pm 4\pi L \gamma$ (described in [53]) and injection in (B.1) and (B.2).
- Injection of the result in (2.17) and (2.18) to obtain the reflected and transmitted signals.

Bibliography

- [1] D. Steck. "Rubidium 85 D Line Data". 2019. url: <https://steck.us/alkalidata/rubidium85numbers.pdf>.
- [2] D. Steck. "Rubidium 87 D Line Data". 2003. url: <https://steck.us/alkalidata/rubidium87numbers.1.6.pdf>.
- [3] D. Steck. "Cesium D Line Data". 2003. url: <https://steck.us/alkalidata/cesiumnumbers.1.6.pdf>.
- [4] D. Steck. "Sodium D Line Data". 2003. url: <https://steck.us/alkalidata/sodiumnumbers.1.6.pdf>.
- [5] T. G. Tiecke. "Properties of Potassium". 2019. url: <https://tobiastiecke.nl/archive/PotassiumProperties.pdf>.
- [6] E. Arimondo, M. Inguscio, and P. Violino. "Experimental determinations of the hyperfine structure in the alkali atoms". In: *Rev. Mod. Phys.* 49 (1 1977), pp. 31–75. doi: 10.1103/RevModPhys.49.31.
- [7] M. E. Gehm. "Properties of ${}^6\text{Li}$ ". 2003. url: <https://physics.ncsu.edu/jet/techdocs/pdf/PropertiesOfLi.pdf>.
- [8] D. Budker, W. Gawlik, D. F. Kimball, S. M. Rochester, V. V. Yashchuk, and A. Weis. "Resonant nonlinear magneto-optical effects in atoms". In: *Rev. Mod. Phys.* 74 (4 2002), pp. 1153–1201. doi: 10.1103/RevModPhys.74.1153.
- [9] S. Bhushan, V. S. Chauhan, M. Dixith, and R. K. Easwaran. "Effect of magnetic field on a multi window ladder type electromagnetically induced transparency with ${}^{87}\text{Rb}$ atoms in vapour cell". In: *Phys. Lett. A* 383.125885 (31 2019). doi: 10.1016/j.physleta.2019.125885.
- [10] M. Bhattarai, V. Bharti, V. Natarajan, A. Sargsyan, and D. Sarkisyan. "Study of EIT resonances in an anti-relaxation coated Rb vapor cell". In: *Phys. Lett. A* 383 (1 2019), pp. 91–96. doi: 10.1016/j.physleta.2018.09.036.
- [11] Z. Tao, M. Chen, Z. Zhou, B. Ye, J. Zeng, and H. Zheng. "Isotope ${}^{87}\text{Rb}$ Faraday filter with a single transmission peak resonant with atomic transition at 780 nm". In: *Opt. Express* 27 (9 2019), pp. 13142–13149. doi: 10.1364/OE.27.013142.
- [12] J. Keaveney, S. A. Wrathmall, C. S. Adams, and I. G. Hughes. "Optimized ultra-narrow atomic bandpass filters via magneto-optic rotation in an unconstrained geometry". In: *Opt. Lett.* 43 (17 2018), pp. 4272–4275. doi: 10.1364/OL.43.004272.
- [13] E. Klinger, H. Azizbekyan, A. Sargsyan, C. Leroy, D. Sarkisyan, and A. Papoyan. "Proof of the feasibility of a nanocell-based wide-range optical magnetometer". In: *Appl. Opt.* 59 (8 2020), pp. 2231–2237.
- [14] R. S. Mathew, F. Ponciano-Ojeda, J. Keaveney, D. J. Whiting, and I. G. Hughes. "Simultaneous two-photon resonant optical laser locking (STROLLing) in the hyperfine Paschen–Back regime". In: *Opt. Lett.* 43 (17 2018), pp. 4204–4207. doi: 10.1364/OL.43.004204.
- [15] D. Sarkisyan, D. Bloch, A. Papoyan, and M. Ducloy. "Sub-Doppler spectroscopy by sub-micron thin Cs vapour layer". In: *Opt. Comm.* 200 (1-6 2001), pp. 201–208. doi: 10.1016/S0030-4018(01)01604-2.
- [16] A. Sargsyan, A. Papoyan, Hughes I. G., C. S. Adams, and D. Sarkisyan. "Selective reflection from an Rb layer with a thickness below $\lambda/12$ and applications". In: *Opt. Lett.* 42 (8 2017), pp. 1476–1479. doi: 10.1364/OL.42.001476.
- [17] A. Sargsyan, G. Hakhumyan, A. Papoyan, D. Sarkisyan, A. Atvars, and M. Auzinsh. "A novel approach to quantitative spectroscopy of atoms in a magnetic field and applications based on an atomic vapor cell with $L = \lambda$ ". In: *Appl. Phys. Lett.* 93.021119 (2008). doi: 10.1063/1.2960346.
- [18] P. Tremblay, A. Michaud, M. Levesque, S. Thériault, M. Breton, J. Beaubien, and N. Cyr. "Absorption profiles of alkali-metal D lines in the presence of a static magnetic field". In: *Phys. Rev. A.* 42 (1990), pp. 2766–2773. doi: 10.1103/PhysRevA.42.2766.
- [19] A. Sargsyan, A. Amiryan, A. Tonoyan, E. Klinger, and D. Sarkisyan. "Circular dichroism in atomic vapors: Magnetically induced transitions responsible for two distinct behaviors". In: *Phys. Lett. A* 390.127114 (2021). doi: 10.1016/j.physleta.2020.127114.
- [20] A. Tonoyan, A. Sargsyan, E. Klinger, G. Hakhumyan, C. Leroy, M. Auzinsh, A. Papoyan, and D. Sarkisyan. "Circular dichroism of magnetically induced transitions for D2 lines of alkali atoms". In: *EPL* 121.53001 (2018). doi: 10.1209/0295-5075/121/53001.
- [21] E. Klinger, A. Sargsyan, A. Tonoyan, G. Hakhumyan, A. Papoyan, C. Leroy, and D. Sarkisyan. "Magnetic field-induced modification of selection rules for Rb D_2 line monitored by selective reflection from a vapor nanocell". In: *Eur. Phys. J. D* 71.216 (2017). doi: 10.1140/epjd/e2017-80291-6.
- [22] A. Amiryan. "Formation of narrow optical resonances in thin atomic vapor layers of Cs, Rb, K and applications". Ph.D Thesis. Université Bourgogne Franche-Comté ; Institute for Physical Research, 2019. url: <https://tel.archives-ouvertes.fr/tel-02318372>.
- [23] A. Sargsyan, A. Amiryan, E. Klinger, and D. Sarkisyan. "Features of magnetically-induced atomic transitions of the Rb D_1 line studied by a Doppler-free method based on the second derivative of the absorption spectra". In: *J. Phys. B: At. Mol. Opt. Phys.* 53.185002 (2020).

- [24] A. Sargsyan, A. Amiryan, and D. Sarkisyan. "Coherent Dicke Narrowing of Absorption Spectra, Collapse and Revival: Second-Derivative Processing". In: *J. Exp. Theor. Phys.* 131 (37 2020), pp. 220–226. doi: 10.1134/S1063776120050179.
- [25] C. Umfer, L. Windholz, and M. Musso. "Investigation of the sodium and lithium D-lines in strong magnetic fields". In: *Z. Phys. D: At. Mol. Clusters* 25 (1992), pp. 23–29. doi: 10.1007/BF01437516.
- [26] H. Hidenobu, M. Masaharu, and D. Muneyuki. "Paschen-Back Effect of D-Lines in Sodium under a High Magnetic Field". In: *J. Phys. Soc. Jpn.* 51.5 (1982), pp. 1566–1570. doi: 10.1143/JPSJ.51.1566.
- [27] R. González-Férez and P. Schmelcher. "Sodium in a strong magnetic field". In: *Eur. Phys. J. D* 23 (2003), 189–199. doi: 10.1140/epjd/e2003-00031-y.
- [28] C.B. Alcock, V.P. Itkin, and M.K. Horrigan. "Vapour Pressure Equations for the Metallic Elements: 298–2500K". In: *Canadian Metallurgical Quarterly* 23.3 (1984), pp. 309–313.
- [29] A.N. Nesmenyanov. *Vapor Pressure of the Chemical Elements*. English edition edited by Robert Gary. Elsevier, 1963.
- [30] W. Demtröder. *Atoms, Molecules and Photons*. Springer-Verlag, 2010.
- [31] G.V. Nikogosyan, D.G Sarkisyan, and Y.P. Malakyan. "Absorption of resonance radiation and fluorescence of a layer of an atomic gas with thickness of the order of a wavelength". In: *J. Opt. Technol.* 71.9 (2004), pp. 602–607. doi: 10.1364/JOT.71.000602.
- [32] G. Dutier, S. Saltiel, D. Bloch, and M. Ducloy. "Revisiting optical spectroscopy in a thin vapor cell: mixing of reflection and transmission as a Fabry–Perot microcavity effect". In: *J. Opt. Soc. Am. B* 20 (5 2003), pp. 793–800. doi: 10.1364/JOSAB.20.000793.
- [33] B. Zambon and G. Nienhuis. "Reflection and transmission of light by thin vapor layers". In: *Opt. Comm.* 143.4 (1997), pp. 308–314. doi: 10.1016/S0030-4018(97)00331-3.
- [34] R. H. Romer and R. H. Dicke. "New Technique for High-Resolution Microwave Spectroscopy". In: *Phys. Rev.* 99 (2 1955), pp. 532–536. doi: 10.1103/PhysRev.99.532.
- [35] E. Tiesinga, P. Mohr, D. Newell, and B. Taylor. "The 2018 CODATA Recommended Values of the Fundamental Physical Constants". In: (2020). url: <http://physics.nist.gov/constants>.
- [36] D. Hanneke, S. Fogwell, and G. Gabrielse. "New Measurement of the Electron Magnetic Moment and the Fine Structure Constant". In: *Phys. Rev. Lett.* 100 (12 2008), p. 120801. doi: 10.1103/PhysRevLett.100.120801.
- [37] A.R. Edmonds. *Angular Momentum in Quantum Mechanics*. Princeton University Press, 1960.
- [38] R.D. Cowan. *The Theory of Atomic Structure and Spectra*. 3rd ed. University of California Press, 1981.
- [39] D.A. Varshalovich, A.N. Moskalev, and V.K. Khersonskii. *Quantum Theory of Angular Momentum*. WORLD SCIENTIFIC, 1988. doi: 10.1142/0270.
- [40] E.B. Alexandrov, M.P. Chaika, and G.I. Khvostenko. *Interference of Atomic States*. Springer-Verlag, 1993.
- [41] G. Breit and I. I. Rabi. "Measurement of Nuclear Spin". In: *Phys. Rev.* 38 (11 1931), pp. 2082–2083. doi: 10.1103/PhysRev.38.2082.2.
- [42] R. Momier, A. Aleksanyan, E. Gazazyan, A. Papoyan, and C. Leroy. "New standard magnetic field values determined by cancellations of ^{85}Rb and ^{87}Rb atomic vapors $5^2\text{S}_{1/2} \rightarrow 6^2\text{P}_{1/2,3/2}$ transitions". In: *J. Quant. Spectrosc. Radiat. Transf.* 257.107371 (2020). doi: 10.1016/j.jqsrt.2020.107371.
- [43] A. Papoyan and S. Shmavonyan. "Signature of optical Rabi oscillations in transmission signal of atomic vapor under continuous-wave laser excitation". In: *Optics Communications* 482 (2021), p. 126561. doi: <https://doi.org/10.1016/j.optcom.2020.126561>.
- [44] D.R. Lide. *CRC Handbook of Chemistry and Physics*. 81st ed. CRC Press, 2000.
- [45] M.P. Bradley, J.V. Porto, S. Rainville, J.K. Thompson, and D.E. Pritchard. "Penning Trap Measurements of the Masses of ^{133}Cs , $^{87,85}\text{Rb}$, and ^{23}Na with Uncertainties ≤ 0.2 ppb". In: *Phys. Rev. Lett.* 83 (22 1999), pp. 4510–4513. doi: 10.1103/PhysRevLett.83.4510.
- [46] W.A. van Wijngaarden and J. Li. "Measurement of hyperfine structure of sodium 3P 1/2,3/2 states using optical spectroscopy". In: *Z. Phys. D* 32 (1994), pp. 67–71. doi: 10.1007/BF01425925.
- [47] R.J. Rafac and C.E. Tanner. "Measurement of the $^{133}\text{Cs}6p^2\text{P}_{1/2}$ state hyperfine structure". In: *Phys. Rev. A* 56 (1 1997), pp. 1027–1030. doi: 10.1103/PhysRevA.56.1027.
- [48] T. Udem, J. Reichert, R. Holzwarth, and T.W. Hänsch. "Absolute Optical Frequency Measurement of the Cesium D_1 Line with a Mode-Locked Laser". In: *Phys. Rev. Lett.* 82 (18 1999), pp. 3568–3571. doi: 10.1103/PhysRevLett.82.3568.
- [49] Wo Yei, A. Sieradzan, and M.D. Havey. "Delayed-detection measurement of atomic Na $3p^2\text{P}_{3/2}$ hyperfine structure using polarization quantum-beat spectroscopy". In: *Phys. Rev. A*. 48 (1993–1915), pp. 1909–1. doi: 10.1103/physreva.48.1909.

- [50] C.E. Tanner and C. Wieman. “Precision measurement of the hyperfine structure of the ^{133}Cs $6P_{3/2}$ state”. In: *Phys. Rev. A* 38 (3 1988), pp. 1616–1617. doi: 10.1103/PhysRevA.38.1616.
- [51] T.A. Vartanyan and D.L. Lin. “Enhanced selective reflection from a thin layer of a dilute gaseous medium”. In: *Phys. Rev. A* 51 (3 1995), pp. 1959–1964. doi: 10.1103/PhysRevA.51.1959. url: <https://link.aps.org/doi/10.1103/PhysRevA.51.1959>.
- [52] S. Briaudeau, S. Saltiel, G. Nienhuis, D. Bloch, and M. Ducloy. “Coherent Doppler narrowing in a thin vapor cell: Observation of the Dicke regime in the optical domain”. In: *Phys. Rev. A* 57 (5 1998), R3169–R3172. doi: 10.1103/PhysRevA.57.R3169.
- [53] E. Klinger. “Selective reflection spectroscopy of alkali vapors confined in nanocells and emerging sensing applications”. Ph.D Thesis. Université Bourgogne Franche-Comté ; Institute for Physical Research, 2019. url: <https://tel.archives-ouvertes.fr/tel-02317761>.